DRAFT VERSION OCTOBER 3, 2021
Typeset using LaTeX **twocolumn** style in AASTeX62

The not so simple stellar system ω Cen. II. Evidence in support of a merging scenario

ANNALISA CALAMIDA,[1] ALICE ZOCCHI,[2] GIUSEPPE BONO,[3,4] IVAN FERRARO,[4] ALESSANDRA MASTROBUONO-BATTISTI,[5] ABHIJIT SAHA,[6] GIACINTO IANNICOLA,[4] ARMIN REST,[1,7] GIOVANNI STRAMPELLI,[8,7] AND ALFREDO ZENTENO[9]

[1]*Space Telescope Science Institute - AURA, 3700 San Martin Drive, Baltimore, MD 21218, USA*
[2]*ESA/ESTEC, Keplerlaan 1, 2201 AZ Noordwijk, Netherlands*
[3]*Dipartimento di Fisica, Università di Roma Tor Vergata, Via della Ricerca Scientifica 1, 000133, Roma, Italy*
[4]*INAF - Osservatorio Astronomico di Roma - Via Frascati 33, 00040, Monteporzio Catone, Rome, Italy*
[5]*Max Planck Institute for Astronomy, Königstuhl 17, D-69117 Heidelberg, Germany*
[6]*National Optical Astronomy Observatory - AURA, 950 N Cherry Ave, Tucson, AZ, 85719, USA*
[7]*Department of Physics and Astronomy, Johns Hopkins University, Baltimore, MD 21218, USA*
[8]*University of La Laguna, Calle Padre Herrera, 38200 San Cristbal de La Laguna, Santa Cruz de Tenerife, Spain*
[9]*Cerro Tololo Inter-American Observatory, Casilla 603, La Serena, Chile*

ABSTRACT

We present multi-band photometry covering $\sim 5^\circ \times 5^\circ$ across ω Cen collected with the Dark Energy Camera, combined to Hubble Space Telescope and Wide Field Imager data for the central regions. The unprecedented photometric accuracy and field coverage allowed us to confirm the different spatial distribution of blue and red main-sequence stars, and of red-giant branch (RGB) stars with different metallicities. The ratio of the number of blue to red main-sequence stars shows that the blue main-sequence sub-population has a more extended spatial distribution compared to the red main-sequence one, and the frequency of blue main-sequence stars increases at a distance of $\sim 20'$ from ω Cen center. Similarly, the more metal-rich RGB stars show a more extended spatial distribution compared to the more metal-poor ones in the outskirts of the cluster. Moreover, the centers of the distributions of metal-rich and metal-poor RGB stars are shifted in different directions with respect to the geometrical center of ω Cen. We constructed stellar density profiles for the blue and red main-sequence stars; they confirm that the blue main-sequence sub-population has a more extended spatial distribution compared to the red main-sequence one in the outskirts of ω Cen, as found based on the star number ratio. We also computed the ellipticity profile of ω Cen, which has a maximum value of 0.16 at a distance of $\sim 8'$ from the center, and a minimum of 0.05 at $\sim 30'$; the average ellipticity is ~ 0.10. The circumstantial evidence presented in this work suggests a merging scenario for the formation of the peculiar stellar system ω Cen.

Keywords: globular clusters: general — globular clusters: Omega Centauri

1. INTRODUCTION

ω Cen (NGC 5139) is the most massive Galactic globular cluster (GGC) with an estimated total mass $M = 2.5 \times 10^6\ M_\odot$ (van de Ven et al. 2006), and more than a dozen stellar sub-populations identified (Bellini et al. 2017c; Milone et al. 2017). ω Cen is unique compared to the other GGCs since its different sub-populations not only show light-element dispersions and anti-correlations, but also a spread of more than 1 dex in iron abundance. Moreover, a dispersion in the heavy element content, including slow neutron-capture (*s*–process) elements, is also present (Norris & Da Costa 1995; Norris et al. 1996; Suntzeff & Kraft 1996; Kayser et al. 2006; Calamida et al. 2009; Johnson & Pilachowski 2010; Marino et al. 2011). Another peculiar property of ω Cen is the split of the main-sequence (MS). Hubble Space Telescope (HST) and Very Large Telescope (VLT) photometry revealed that ω Cen MS bifurcates in two main components, the so called blue MS (bMS) and red MS (rMS, Anderson 2002; Bedin et al. 2004; Sollima et al. 2007b). Spectroscopic follow-up by Piotto et al. (2005) showed that bMS stars might be slightly more metal-rich than rMS stars, and thus it was suggested that bMS stars constitute a helium-enhanced sub-population in the cluster.

A study based on the spectroscopic abundances of ~ 500 red-giant branch (RGB) stars combined with radial veloc-

Corresponding author: Annalisa Calamida
calamida@stsci.edu

ities unveiled that ω Cen stellar sub-populations have different kinematical properties: the metal-rich (MR) stars do not share the rotational velocity (maximum line-of-sight rotational velocity on the major axis, V $\sim$ 8 km s^{-1}, van de Ven et al. 2006) of the metal-poor (MP) component, and the most MR RGBs seem to have a smaller velocity dispersion than the MP ones (Norris et al. 1997). However, these results were later questioned by Pancino et al. (2007) and Sollima et al. (2009), who found that the most MR stellar component of ω Cen does not present any significant radial velocity offset with respect to the bulk of stars. The velocity dispersion of the cluster appears to decrease monotonically from $\sigma_v \sim 17.2$ km/s down to a minimum value of $\sigma_v \sim 5.2$ km/s, in the region $1.5 \leq r \leq 28'$ (where the half-mass and tidal radii are $r_h = 5$ and $r_t = 57'$, respectively Harris 1996). For distances larger than $30'$, a hint of a raise in the velocity dispersion is present, but this result is not statistically significant (Sollima et al. 2009).

A proper motion study of different stellar sub-populations in ω Cen was performed by Ferraro et al. (2002), and showed that the most MR stars in the cluster have a different motion compared to the metal-intermediate (MI) and MP stars: the proper-motion centroid for the MR stars is offset from the centroid of the MP stars. The authors suggested that the most MR stars in ω Cen formed in an independent stellar system that was later accreted by the cluster. However, these results have not been confirmed in the study presented by Platais et al. (2003), who suggested that the observed proper motion shift could be due to a residual color- or magnitude-dependent term in the proper motions, and by Bellini et al. (2009), who performed a similar analysis on a different data set. These works found no difference between the global proper motions of stellar sub-populations with different metallicity.

Pancino et al. (2000, 2003) found that the three main stellar sub-populations of ω Cen (MP, MI, and MR) have different spatial distributions: MP RGB stars extend along the direction of the cluster major axis (East-West), while the MI and MR along the North-South axis in the center and they are elongated East-West in the outskirts. This result was confirmed by Hilker & Richtler (2000), based on Strömgren photometric metallicities for a sample of ω Cen RGBs. In particular, they found that the more MR stars seem to be more concentrated within a radius of $10'$. Sollima et al. (2005a) also found that MR RGB stars are more centrally concentrated, by using photometry for a field of view of $\approx 0.2^\circ \times 0.2^\circ$ across ω Cen.

In a recent work based on Dark Energy Camera (DECam) observations covering $\sim 2^\circ \times 2^\circ$ across ω Cen, we found that the frequency of bMS stars increases compared to rMS stars in the outskirts of the cluster (Calamida et al. 2017, hereafter CA17). Furthermore, we also showed that stars of another sub-population in ω Cen, the reddest and most metal-rich RGB, have a more extended spatial distribution in the outskirts of the cluster, a region that was not explored in previous studies. bMS stars should also be more metal-rich compared to the cluster main stellar population, according to the spectroscopic measurements of Piotto et al. (2005). Therefore, these findings make ω Cen one of the few stellar systems currently known where metal-rich stars have a more extended spatial distribution compared to metal-poor stars. A similar behavior has been observed in the cluster M 80, where Dalessandro et al. (2018) found that the stellar sub-population enriched in Sodium (Na) and depleted in Oxygen (O), which they identify as the second generation, has a more extended spatial distribution compared to the cluster main stellar sub-population (the first generation), which is Na-poor and O-rich. The authors claimed that the two stellar sub-populations have a different helium content and this causes a mass difference, resulting in spatial segregation of the stars, with the lower mass second-generation stars having a more extended spatial distribution.

A similar case is the GGC M 22, where two main groups of stars were identified, the Calcium weak ($Ca-w$) and the Calcium strong ($Ca-s$): the $Ca-w$ stars are more centrally concentrated, and the $Ca-s$ stars have a more extended spatial distribution at larger radii (Lee 2015). The $Ca-w$ and $Ca-s$ stellar sub-populations have their own light-element anti-correlations and they also show a mild iron abundance difference, $\Delta[Fe/H] \sim 0.15$ dex, with the $Ca-s$ stars being more metal-rich compared to the $Ca-w$ stars (Marino et al. 2009, 2011). To explain the origin of the spatial distribution of the stellar sub-populations in M 22, a scenario where two clusters with slightly different metallicities merged was proposed by Lee (2015). A merger scenario was also advanced for another peculiar GGC, NGC 1851, which shows a similar small spread in the iron abundance, $\Delta[Fe/H] \sim$ 0.06-0.08 dex, with the two stellar sub-populations having different s–process and light-element abundances and the more MP stars more concentrated compared to the more MR stars (Yong & Grundahl 2008; Carretta et al. 2010, 2011). This GGC also has a stellar halo and possibly tidal tails (Olszewski et al. 2009; Carballo-Bello et al. 2017; Kuzma et al. 2018).

The formation history of ω Cen could be more complex than that of these GGCs, due to the presence of a very large iron abundance spread and the numerous stellar sub-populations observed. The two current main scenarios to explain the origin of ω Cen are that this peculiar stellar system is the nucleus of a dwarf galaxy accreted by the Milky Way or the result of the merger of two or more clusters (Norris et al. 1997; Jurcsik 1998; Bekki & Freeman 2003; Pancino et al. 2000; Bekki & Norris 2006). The merger could have happened in a dwarf galaxy,

where cluster encounters are more frequent than in the Galactic halo due to the lower velocity dispersion, and the system could have been later accreted by the Milky Way (Thurl & Johnston 2002). Different works have recently simulated the merging of clusters in dwarf galaxy environments to explain the origin of GGCs with iron and light-element abundance spread (Amaro-Seoane et al. 2013; Bekki & Tsujimoto 2016; Gavagnin et al. 2016; Pasquato & Chung 2016), and some of them are very successful in reproducing the current properties of ω Cen. Mastrobuono-Battisti et al. (2019) used simulations to show that GGCs in the disk and bulge, such as Terzan 5, may result from encounters and subsequent merging and mass exchanges between a primordial population of clusters.

In support of the merger scenario for the origin of ω Cen is the different spatial distribution and kinematics of the MP and MR RGB stars, and the different spatial distribution of the blue and red MS stars. We now push forward the ongoing investigation to better understand the origin of ω Cen with precise multi-band DECam photometry covering $\sim 5^\circ \times 5^\circ$ across the cluster. The larger field of view allows us to study the spatial distribution of the different sub-populations in ω Cen until and beyond the tidal radius. The deep and accurate wide-field DECam photometry, covering the entire extent of the cluster, combined to HST photometry for the core, also allows us to accurately characterize the density profile of ω Cen and of its different sub-populations. The analysis of these structural properties will help us to shed light on the origin of this mysterious stellar system.

The structure of the current paper is as follows. In §2 we present the new DECam observations and how we derived the latest photometric catalog. In §3 we discuss the spatial distribution of the blue and red MS and in §4 we analyze ω Cen stellar density profiles and derive its ellipticity. In §5 we study the spatial distribution of RGB stars with different metallicities and in §6 we discuss the results. §7 summarizes the results and presents the conclusions.

2. THE PHOTOMETRIC CATALOG

A set of 342 *ugri* images centered on ω Cen was collected over four nights, 2014 February 24, 2015 June 22, 2016 March 4, and 2017 April 15 with DECam on the Blanco 4m Telescope (CTIO, NOAO). DECam is a wide-field imager composed of 62 detectors (61 operational) and covers a 3 square degree sky field of view (FoV) with a pixel scale of $0.263''$. Data collected in the first 3 nights were published in CA17; the current work is based on those with the addition of DECam images collected in 2017.

Exposure times for our observations ranged from 120 to 600s for the *u* and from 7 to 250s for the *gri* filters. Weather conditions were very good for all nights with image seeing ranging from $0.8''$ to $1.6''$ for the *u* and from $0.7''$ to $1.2''$ for the *gri* filters. Standard stars from the Sloan Digital Sky Survey Stripe 82 were observed in all filters and at different air masses during the night of February 2014. The FoV centered on ω Cen was observed during the 2014, 2015 and 2016 runs, and four new fields were added in the 2017 run to cover a larger area around the cluster. Fig. 1 shows the footprint of the combined DECam photometric catalog for ω Cen. Note that while detector S7 currently works, N7 is still not operational and stars are missing at the bottom of the DECam footprint.

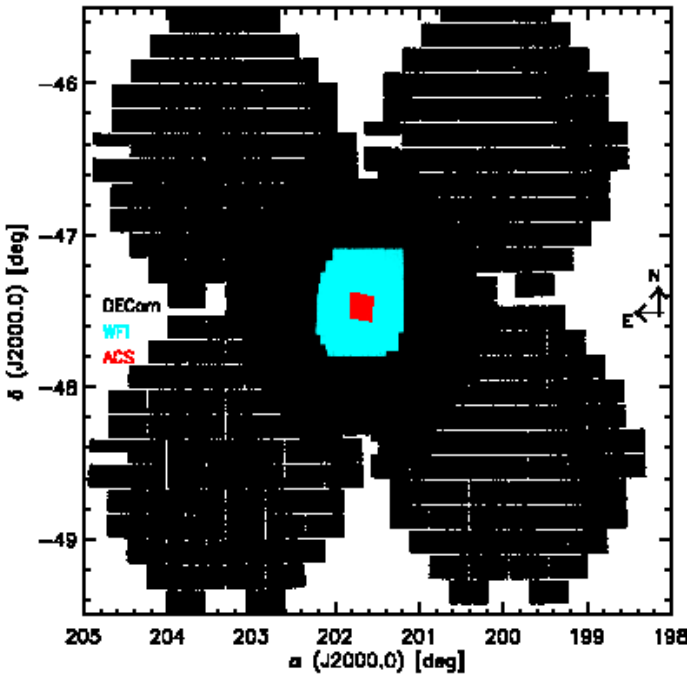

Figure 1. Field of view covered by DECam photometric catalog across ω Cen (black dots). The orientation is labeled in the figure. Detector N7 is not operational and stars are missing at the bottom of the DECam fields. Cyan and red dots indicate stars observed in the WFI and ACS field of views, respectively. See text in § 4 for more details.

Photometry on images for the four new DECam fields was performed with DoPHOT (Schechter et al. 1993; Saha et al. 2010), following the same prescriptions used to reduce DECam central field in CA17, and applying the same zero points to calibrate the photometry. The accuracy of the photometric calibration ranges between 2% for the *r* and *i* filters to 4−5% for the *g* and *u* filters. The old and new DECam catalogs were combined and the final catalog includes $\sim 1.4\times10^7$ stars and covers a FoV of $\approx 5^\circ\times5^\circ$centered on ω Cen (see Fig. 1).

The left panel of Fig. 2 shows the i, $g-i$ color-magnitude diagram (CMD) for all stars observed in the FoV towards ω Cen. The CMD is still heavily contaminated by field stars, mostly thin/thick disk and halo stars. To separate field and cluster stars we used the same approach adopted in CA17, i.e.

we estimated the ridge lines of the different sub-populations identified along the cluster RGB, the main sequence turn-off (MSTO) and the MS in the color-color-magnitude diagram $u-r$ vs $g-i$ vs r. Once the ridge lines were estimated we performed a linear interpolation among them and generated a continuous multi-dimensional surface. Finally, we used different statistical parameters to separate field and cluster stars. For more details on the procedure we refer to CA17.

After cleaning the catalog from field stars we are left with 432,295 candidate ω Cen members. In order to verify the cluster and field star separation, we took advantage of the Gaia DR2 catalog (Gaia Collaboration et al. 2018). ω Cen is one of the clusters with the worst accuracy of the five astrometric parameters provided by the release, i.e. positions, proper motions and parallax. As shown in Fig. A.6 of Gaia Collaboration et al. (2018), the selection of well-measured stars produces holes in the coverage of the cluster (see also Bianchini 2019 for a detailed discussion on the accuracy of Gaia measurements for ω Cen). Moreover, reliable Gaia astrometric and photometric measurements are provided only down to $G \sim 20$ mag, about 1 magnitude below ω Cen MSTO. The focus of this work is to study the spatial distribution of the blue and red MS down to $G \sim$ 22.5 mag, and the two sequences cannot be accurately measured and separated with Gaia photometry and astrometry. We matched our catalogs of cluster and field members with Gaia, by using a searching radius of 0.5″, and we used the proper motion plane to estimate how many stars might have been misidentified with our method. In order to only use stars with the best quality parameters in the Gaia astrometric catalog, we limited our analysis to stars brighter than i = 16.0 mag, ending up with 10,110 and 34,524 candidate ω Cen and field stars, respectively, out of which 7,849 and 32,957 have proper motion measurements in Gaia. Gaia proper motion for ω Cen is μ_α = -3.1925±0.0022 and μ_δ = -6.7445±0.0019 mas/yr (Gaia Collaboration et al. 2018) and we selected as candidate cluster members stars with -6.0 $< \mu_\alpha <$ 0 and -10 $< \mu_\delta <$ -3.5 mas/yr. Of the 7,849 stars selected as ω Cen members with our color-color-magnitude method, 662 are field stars according to Gaia proper motions, i.e. $\sim$ 8%. We repeated the same procedure for stars selected as field members from the color selection and less than 1% are candidate cluster stars according to proper motions. We can thus conclude that the color-color-magnitude method is a powerful tool to disentangle cluster and field stars in the absence of accurate proper motions down to faint magnitudes. Photometric accuracy hampers the color selection at fainter magnitudes, but nevertheless the fraction of cluster stars lost with this method is negligible, while the residual contamination of field stars is $\lesssim$ 10%, and affects the blue and red MS sample in the same way (see also CA17).

Candidate ω Cen members are plotted in the $i,\ g-i$ CMD shown in the right panel of Fig. 2. The CMD in the right panel of Fig. 2 shows that all the cluster sequences are well-defined, including the extreme horizontal branch (EHB) at $g-i \sim$ -0.7 and 18 $< i <$ 20 mag. Photometry reaches $i \approx$ 22.5 mag with $S/N \approx 20$ and $i \approx 21$ mag with $S/N \approx 70$.

Fig. 3 shows a zoom of the $i,\ g-i$ CMD in the magnitude and color ranges 16.5 $< i <$ 21 and 0.2 $\leq g-i \leq$ 1.2. The MS split is clearly visible: the bMS and the rMS start to separate at $i \approx$ 18.5 mag, and their color distance increases at fainter magnitudes. A third less populated and redder sequence is also visible, the so-called MS-a. This sequence connects to ω Cen faintest sub-giant branch, the so-called SGB-a (Ferraro et al. 2004), and to the reddest RGB, the so-called RGB-a by Pancino et al. (2000) or ω3 by us (Castellani et al. 2007), which are not visible in this CMD. It is worth noticing that the bMS and the rMS intersect at $i \approx$ 18.5 mag and the rMS continues onto ω Cen brighter SGB, while the bMS should connect to a fainter SGB. Very accurate multi-band HST photometry enables a more clear view of the multiple ω Cen turn-off (TO) points and how they connect to the multiple MSs and RGBs (Bellini et al. 2017a); however, it is not clear yet which SGB and RGB are the continuation of the bMS.

The astrometric calibration of ω Cen DECam catalog to the equatorial system J2000 was performed as described in CA17 and has a precision better than 0.03″ in both right ascension and declination. We then converted the equatorial coordinates, α and δ, to cartesian coordinates by following the prescriptions of van de Ven et al. (2006), with the cluster center at α_0 = 201.694625° and δ_0 = -47.48330° (Braga et al. 2016), setting x in the direction of West and y in the direction of North. We then rotated the cartesian coordinates x and y by the position angle of ω Cen, 100° (van de Ven et al. 2006), resulting with x-axis and the y-axis aligned with respectively the observed cluster major and minor axis.

3. THE BLUE AND RED MS SPATIAL DISTRIBUTION

ω Cen MS splits in two main sequences, the bMS and rMS, as shown in Fig. 3. The MS split was first identified with HST photometry by Anderson (2002) and Bedin et al. (2004), and later confirmed with VLT observations by Sollima et al. (2007b) and with DECam data by CA17. Piotto et al. (2005) observed 17 stars distributed on the blue and on the red MS: the spectra showed that bMS stars are $\sim$ 0.3 dex more metal-rich than rMS stars, counter to expectations given their bluer color. However, these spectra have very low S/N ($\lesssim$ 3 for individual spectra and $<$ 30 for the co-added) and additional data are necessary to confirm these results. Following these spectroscopic results, Piotto et al. (2005) proposed that bMS stars constitute a helium-enhanced sub-population as an explanation of the observed anomaly.

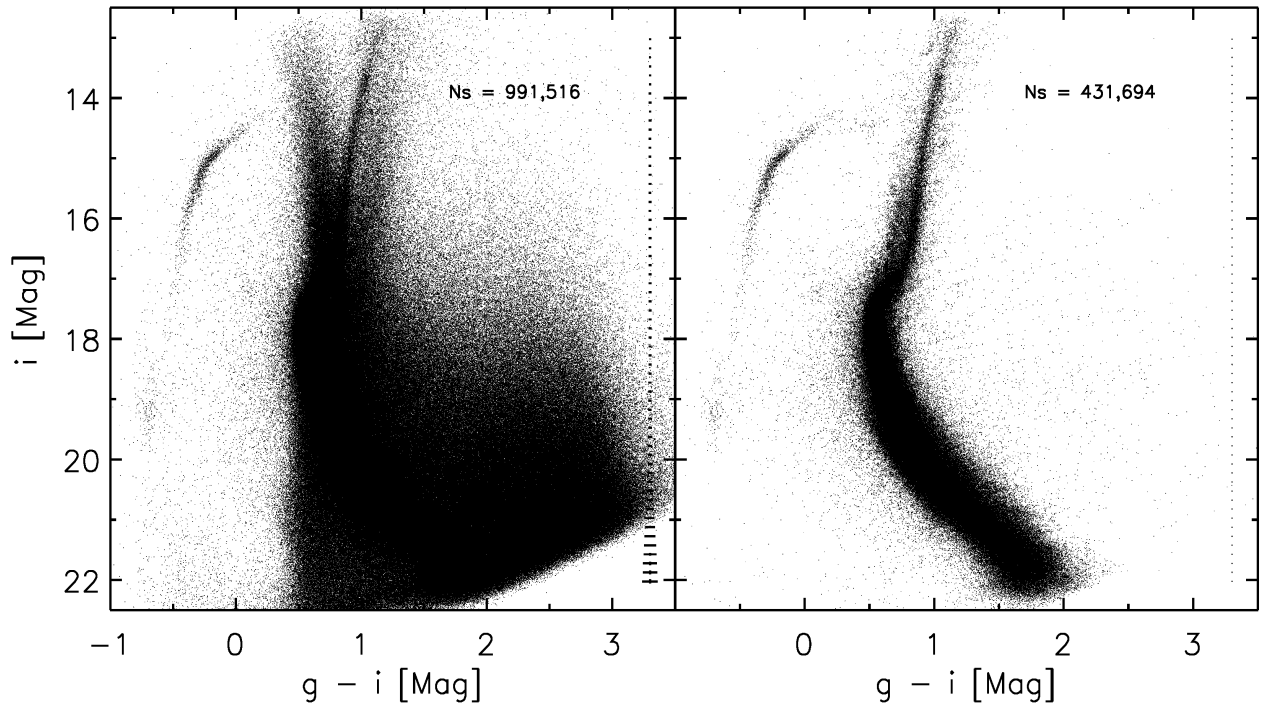

Figure 2. Left: DECam *i, g-i* color-magnitude diagram towards ω Cen. Error bars are shown. – Right: same plot but for selected cluster members.

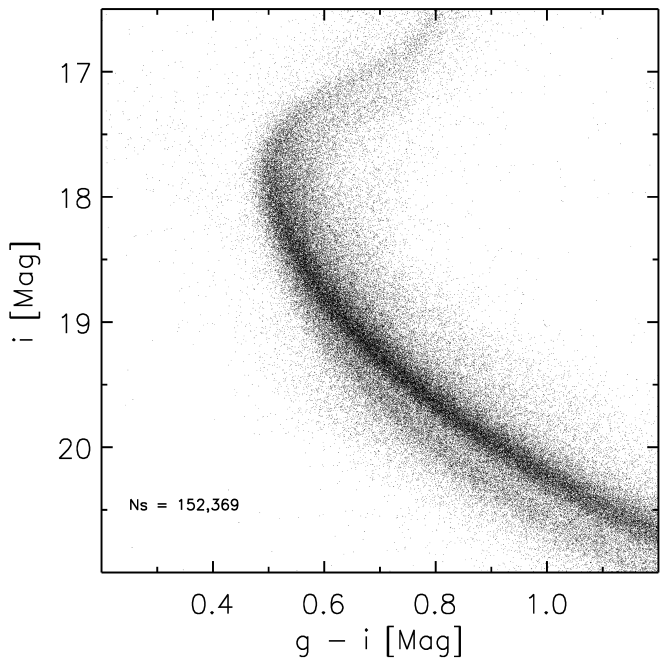

Figure 3. Zoom of the DECam *i, g-i* color-magnitude diagram of ω Cen selected cluster members. The split of the MS is clear: the bMS and the rMS start to separate at $i \sim 18.5$ mag and their separation increases at fainter magnitudes. See text for more details.

CA17 performed an analysis of the spatial distribution of bMS and rMS stars in ω Cen, finding that bMS stars are more concentrated compared to rMS stars until $\approx 25'$ from the cluster center, and that they show a more extended distribution at larger distances. Moreover, they found that the frequency of bMS stars, supposedly more metal-rich than the rMS stars according to the spectroscopic measurements available, steadily increases at larger distances.

With the extended DECam photometric catalog, we can now better characterize the distribution of bMS and rMS stars in the vicinity of the truncation radius and beyond ($r_t \sim 1.0°$, Harris 1996). To achieve this goal, we computed the ratio of the number of bMS and rMS stars, $R(bMS/rMS) = N(bMS)/N(rMS)$, as a function of the radial distance, r. In order to select the sample of blue and red MS stars in the $19.25 < i < 20.5$ magnitude range, where the two sequences better separate, we used the same procedure illustrated in CA17. The samples of blue and red MS stars were selected for different $g-i$ color bins, Δ, after the two main sequences were rectified by subtracting to each star the color of the bMS or rMS ridge line. The minimum color bin for the selection was $\Delta = 0.02$ mag, equal to the color uncertainty in the selected magnitude range, and the maximum bin was $\Delta = 0.20$ mag, for a total of 18 bins. Note that with this selection the bMS and rMS samples never overlap (see Fig. 9 in CA17).

Fig. 4 shows the 3D plot of $R(bMS/rMS)$ as a function of the radial distance, r, in arcminutes, and of the $g-i$ color bin,

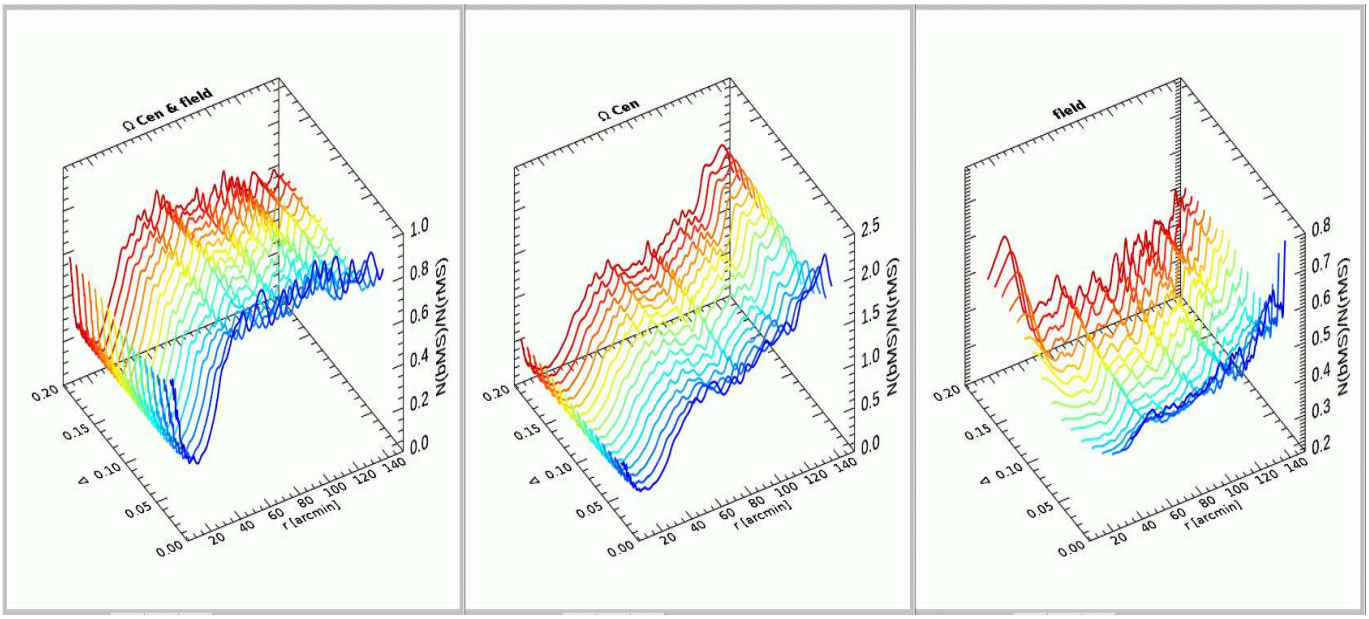

Figure 4. Ratio of the number of bMS and rMS stars, $N(bMS)/N(rMS) = R(bMS/rMS)$ as a function of distance from the cluster center, r, and the $g-i$ color bin used to select the stars, Δ. The three panels show the same ratio for all the stars (left), for candidate cluster members only (middle) and for candidate field members only (right), in the magnitude interval $19.25 < i < 20.5$.

Δ, used in the selection for the entire sample of stars included in the $19.25 < i < 20.5$ magnitude interval (left panel), for only the candidate cluster stars (middle), and for the candidate field stars only (right). The different $g-i$ color selections are plotted with arbitrary colors to highlight the difference when moving from narrower to wider color bins.

Fig. 5 shows the ratio of the number of bMS and rMS stars as a function of distance for the largest color bin, $\Delta = 0.2$ mag, and for $0.1'$ distance bins from ω Cen center. From Figs. 4 and 5 it is clear that $R(bMS/rMS)$ decreases from a distance of $\approx 10'$ from the center down to a minimum, $R(bMS/rMS) \sim 0.18$, at a distance $r \sim 20'$ (marked with a solid line in Fig. 5), and then it starts to increase. The ratio then reaches a local maximum, $R(bMS/rMS) \sim 0.85$, at $r \sim 60'$ (solid line in Fig. 5) and it stays approximately constant at larger distances. From a distance from the cluster center of $\sim 100'$ the ratio starts to increase again until the largest distance sample of $\sim 140'$. Error bars in Fig. 5 indicate the uncertainties, calculated as Poisson error on the star counts.[1]

$R(bMS/rMS)$ at the center of the cluster is not sampled by DECam data: Bellini et al. (2009), Sollima et al. (2007b), and later CA17, showed that the ratio has values in the interval 0.2–0.5 in between 0 and $10'$ from the cluster center.

It is worth mentioning that these findings are independent of the $g-i$ color bin used to select the sample of bMS and rMS stars and indeed the radial trends are quite similar when moving from the narrower to the wider bin as shown in Fig. 4. Moreover, the current finding is also independent of the approach used to select candidate cluster and field stars. The population ratios are similar in the left panel of Fig. 4, where the ratio is the entire sample of stars, and in the middle panel, where it is based on candidate cluster members only.

Data plotted in the middle panel of Fig. 4 and in Fig. 5 show that a local maximum in the population ratio is attained in the outskirts of ω Cen at about the truncation radius, $r \sim 60'$, where the ratio of bMS to rMS stars is of the order of 0.85. This value is smaller than the ratio found with the previous DECam dataset by CA17 at the same distance. In the previous work, the result was affected by a lack of statistics at these distances from the cluster center, since the photometric catalog was only based on data for DECam central field (see Fig. 1). At larger distances, the bMS stars dominate over the rMS stars, reaching another local maximum at $r \sim 115'$, where the ratio is of order of 1.2 (solid line in Fig. 5).

The population ratios based on only candidate field stars plotted in the right panel of Fig. 4 show an approximately flat trend from the inner to the outer cluster regions for the smaller $g-i$ color bins, while an increase is observed for wider bins, with $R(bMS/rMS) \sim 0.7$ for $r < 30'$, compared to the approximately flat value of $R(bMS/rMS) \sim 0.5$ in the more external regions. As discussed in §2, a small ($\sim 1\%$) fraction of cluster stars might have been classified as field stars and might cause the increase of the ratio towards the cluster center.

In CA17 we have already demonstrated how our result, confirmed here with the extended photometric catalog, is not

[1] We calculated the uncertainties as Poisson errors in the following way: $\sigma = (N(bMS)/N(rMS)) \times \sqrt{\frac{N(bMS)+N(rMS)}{N(bMS)\times N(rMS)}}$

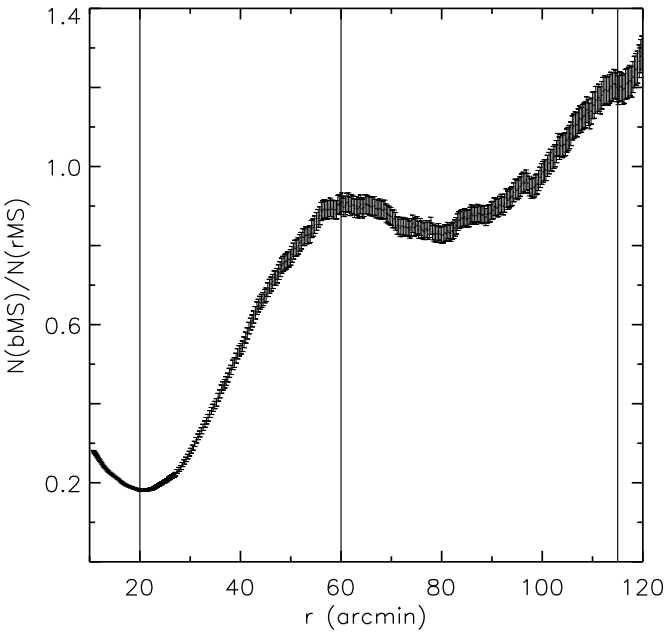

Figure 5. Ratio of the number of bMS and rMS stars as a function of distance from the cluster center and for a $g-i$ color bin $\Delta = 0.20$ mag, calculated in bins of $0.1'$ width. Error bars are shown. The vertical lines indicate the approximate distance at which the ratio reaches its local minimum and maximum values. See text for more details.

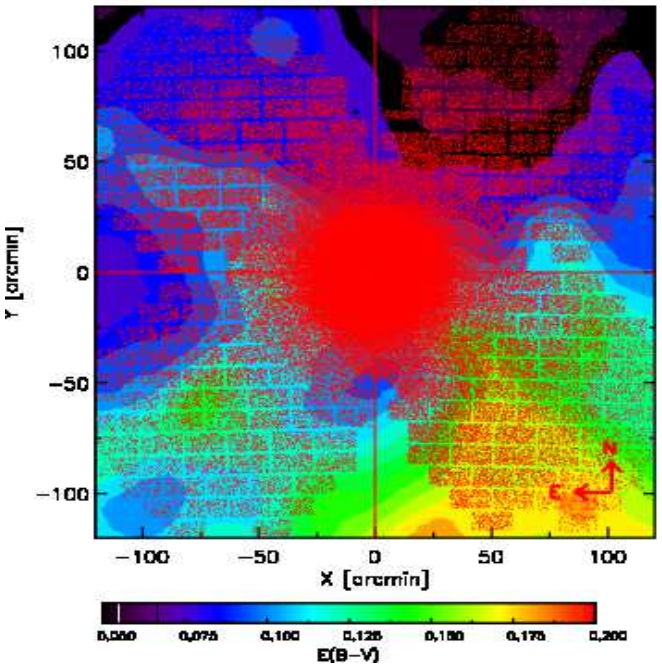

Figure 6. Reddening color density map as derived from Schlafly & Finkbeiner (2011) for stars towards the observed region across ω Cen. Stars identified as ω Cen members from DECam photometric catalog are over-plotted as red dots. The North and East direction are indicated with red arrows.

affected by foreground reddening. To further constrain this issue, we used reddening values from Schlafly & Finkbeiner (2011) for the observed field of view towards ω Cen. The map of the derived $E(B-V)$ values is shown in Fig. 6: a decrease of the extinction in the Northern half of the cluster and an increase in the South-West quadrant is evident, with values ranging from a minimum of $E(B-V) \sim 0.05$ to a maximum of $E(B-V) \sim 0.2$ mag. However, the extinction averages around $E(B-V) \sim 0.11$ mag, with a 1-σ dispersion of 0.025 mag. These values are in very good agreement with the dispersion $\sigma_{E(B-V)} \lesssim 0.03$ mag found by Cannon & Stobie (1973) and Calamida et al. (2005), and $\sigma_{E(B-V)} \lesssim 0.04$ mag found by Bellini et al. (2017b), and based on photometric studies of ω Cen.

As shown in CA17 for a smaller field of view, the presence of some differential reddening or an increase in the extinction in some regions in the outskirt of ω Cen would cause a decrease in the population ratio, $R(bMS/rMS)$, since stars truly belonging to the bMS will be moved into the rMS sample. Therefore, the observed increase in the population ratio, i.e. the increase of the number of bMS stars towards the outskirts of the cluster, cannot be due to the presence of some differential reddening. Indeed, this low differential reddening could move stars from the blue to the red MS samples, but it cannot explain the over-abundance of bMS stars at larger distances from ω Cen center.

Our results agree very well with the findings of Sollima et al. (2007b) for distances larger than $10'$ and up to $r \approx 25'$, i.e. the cluster region sampled by this work, also confirming what found in CA17. On the other hand, our results do not agree with those of Bellini et al. (2009) for this region of ω Cen: our ratio of bMS and rMS stars is significantly lower than the ratio found by them. At $r \approx 15'$, for example, Bellini et al. (2009) found a ratio of 0.36 ± 0.04, while our ratio is 0.220 ± 0.002, more than 3σ smaller. This discrepancy can be explained by taking into account their different selection of bMS and rMS stars with respect to this work. Our sample of rMS stars is contaminated by unresolved binaries and by MS-a stars. Photometric and spectroscopic analyses provide a binary frequency for ω Cen of $\approx 5\%$ (Mayor et al. 1996; Sollima et al. 2007a), and MS-a stars, which are the counterpart of RGB-a stars, are less than 5% of cluster stars (Pancino et al. 2000, CS07). These factors will cause an artificial increase in the star counts of the rMS, i.e. a decrease of the absolute value of the bMS to rMS number ratio. By accounting for these factors, our population ratio would agree with the findings of Bellini et al. (2009). However, these factors cannot explain the global decreasing trend with distance of the ratio of bMS and rMS stars observed with DECam data and not found by Bellini et al. (2009): the number of binaries is expected to decrease at increasing distances from the cluster center, and the MS-a stars are more centrally con-

centrated compared to metal-poor stars (Pancino et al. 2003; Bellini et al. 2009, CA17). Because th number of these objects decreases at larger distances from the cluster center, we would expect an increase of the bMS to rMS ratio. However, DECam data clearly show that this population ratio decreases from $\sim$10′ up to a distance of $\approx$ 20′, as previously also shown by Sollima et al. (2007b). Bellini et al. (2009) and Sollima et al. (2007b) did not analyze the bMS to rMS star ratio for distances larger than $\sim$ 20′, so we cannot compare our results for this region of ω Cen; Sollima et al. (2007b) observed a slight increase of the population ratio for distances larger than 20′ from the cluster center, but they pointed out that these results are not statistically significant (see their Fig. 7). DECam data presented in CA17 and in this work finally allowed us to study the population ratio and the spatial distribution of the bMS and rMS sub-populations for distances larger than 20′ and until the tidal radius and beyond, a region that was never explored before.

4. STELLAR DENSITY PROFILES

We took advantage of the coverage and depth of DECam photometric catalog to study the stellar density profile of the bMS and rMS sub-populations. We then combined DECam photometry to the ACS and WFI datasets to cover the more internal regions of ω Cen, and to determine the global stellar density profile of the cluster to compare it with the bMS and rMS profiles. The stellar density profile we present here for ω Cen includes, for the first time, star counts of TO, MS, sub-giant branch (SGB), and RGB stars. MS stars are approximately a factor of 100 more numerous than the brighter RGB stars, and thus they provide a more reliable description of the cluster density profile, particularly at larger distances from the center, where the star density declines.

We used DECam photometry for ω Cen cluster members for distances larger than 16′ from the center, i.e. about three times the half-mass radius. At these distances, DECam photometry is not affected by crowding, and the catalog can be considered more than $\sim$ 90% complete down to $r \sim 20$ mag, where $S/N \sim 200$. For distances $r < 16'$, we used Advanced Camera for Surveys (ACS) HST data and the Wide Field Imager (WFI) on the MPG 2.2m ESO telescope photometry published in Castellani et al. (2007). These datasets cover the innermost regions of ω Cen (see the footprints in Fig. 1): in particular, ACS covers a radial distance from $\sim$ 1 to 4′ (red dots in Fig. 1), while WFI covers a radial distance from $\sim$ 4 to 16′ (cyan dots). The three photometric catalogs were matched together and the combined catalog includes 1.8×10^7 cluster stars measured in 11 filters ($F475W, F625W, F658N$, U, B, V, I, u, g, r, i). The ACS $F625W-$band photometry was transformed to DECam $r-$band by comparing photometry of stars in common between the two catalogs. We found that $r_{DECam} = F625W - 0.2$. For the WFI dataset, we transformed the $V-$ and $I-$band photometry to $F625W$ following the prescription of Castellani et al. (2007), i.e. $F625W = V \times 0.544 + I \times 0.455$, and then to DECam $r-$band as described. To take into account the different completeness levels of the photometric catalogs and the saturation of the ACS catalog at brighter magnitudes, we only selected ω Cen stars in the magnitude range $14.5 < r < 20$ mag, i.e. from the RGB down to approximately 3 magnitudes below the MSTO. Stars were then divided in circular annuli with width of 0.5′, from a distance of 1′ from the cluster center until 100′; to increase the number statistics in the spare outermost regions of the cluster we selected stars in bins of 1′ from 100 to 140′. The number of stars per bin was divided by the area of the annulus to obtain the number density of stars as a function of distance from the cluster center, which is shown with green filled circles in Fig. 7.

We performed the same analysis for the bMS and rMS stars for distances larger than 16′ from ω Cen center. In this case, we used the samples selected for a $g-i$ color bin of 0.2 mag. The bMS and rMS stars have the same completeness level since they were selected in the same magnitude range ($19.25 < i < 20.5$ mag). These profiles were then stitched to the inner part of the global stellar density profile (at distances $r < 16'$), after an appropriate normalization. Fig. 7 shows the resulting density profiles computed for the global (green filled circles), rMS (red) and bMS (blue) cluster stellar populations. From this figure, it appears that bMS stars are slightly more concentrated compared to rMS stars until $\sim$20′; outside this radius, the bMS stars density is larger compared to the rMS stars density, supporting the results obtained with the bMS to rMS star ratio. In Appendix A we show the results of the fits we carried out with dynamical models with different truncation prescriptions to these profiles, to capture their different behaviors in the outermost regions of ω Cen.

Thanks to the unprecedented combination of data used here, we can also investigate additional properties of the stellar distribution of this cluster. In particular, in this Section we discuss the possible presence of a halo of stars in the outermost regions and we compute a new ellipticity profile for ω Cen.

4.1. *A stellar halo and/or tidal tails*

In the past, Leon et al. (2000) used star counts to claim the presence of tidal tails around ω Cen, extending perpendicularly to the Galactic plane. However, this result was questioned by Law et al. (2003), who showed that those star counts were affected by variable extinction towards ω Cen. In a more recent work, we used OmegaCam on the VST telescope (ESO) to study the number density profile of ω Cen (Marconi et al. 2014). The VST photometry was 2.5 magnitude shallower compared to our current DECam pho-

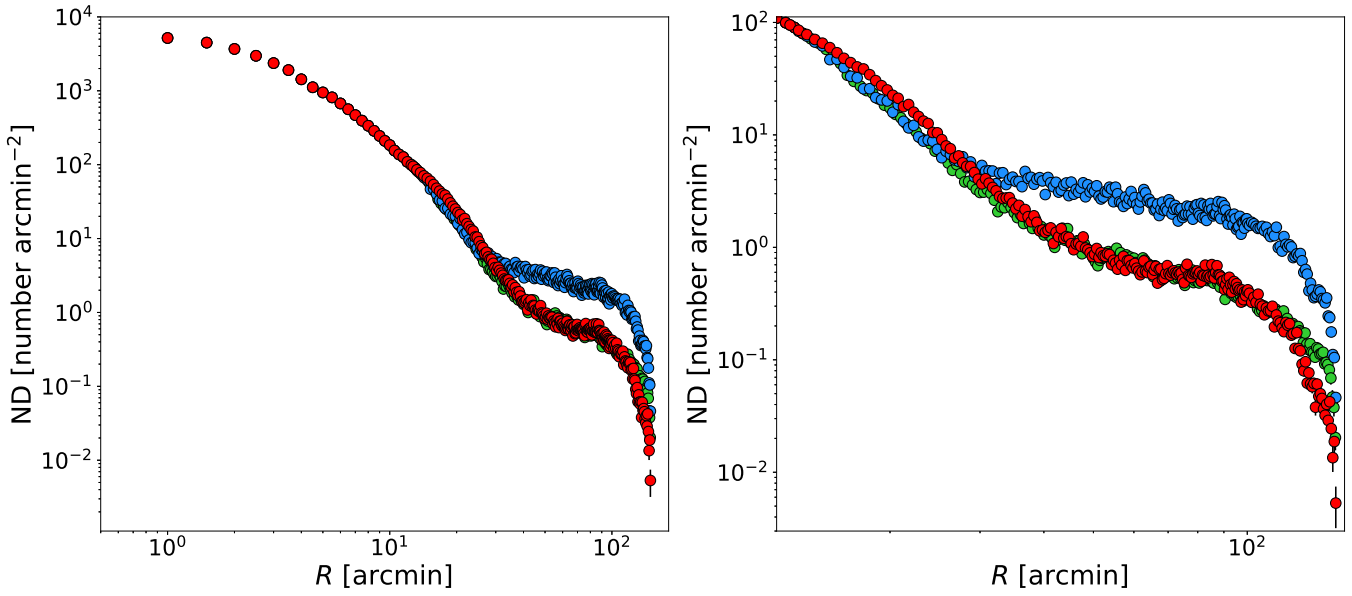

Figure 7. Left: Number density profile for all selected cluster members (green circles) and for selected bMS (blue) and rMS stars (red); error bars are shown. The innermost part of these profiles is the same, as described in the text; differences among the rMS and bMS star density are evident when looking at distances $\gtrsim 20'$. Right: zoomed version of the plot to highlight the differences in the outermost parts of the profiles.

tometry, and only three filters, *gri*, were available. Therefore, we were not able to use the color-color-magnitude method to separate cluster and field stars. In order to analyze the stellar density profile, stars were selected for a narrow magnitude and color range across ω Cen MSTO and the SGB. The number density profile showed the presence of two over-densities of stars at $\approx 1^\circ$ from ω Cen center in the North - West quadrant and at $\approx 2^\circ$ in the opposite South-East quadrant (see Fig. 22 in Marconi et al. 2014). However, these results could have been affected by field star contamination. More recently, Ibata et al. (2019) identified tidal tails extending up to 28° from ω Cen based on Gaia DR2 data, oriented in the same North-West – South-East direction, starting from a distance of 100′ from the cluster center, confirming the results of Marconi et al. (2014).

We then used the combined ACS+WFI+DECam photometric catalog to investigate the presence of asymmetries in the stellar density profiles. We selected only stars in the North-West – South-East direction (tidal tail direction) and the opposite one, and produced a density profile considering all stars, bMS, and rMS stars in both directions. These new profiles show no significant difference in the distribution of stars along different directions; we fit them with the dynamical models presented in Appendix A and we found best-fit parameters in very good agreement, within uncertainties, with the ones obtained for the global profiles and reported in Table2.

To further investigate the presence of asymmetries in the stellar density profiles, we divided the clusters in 15-degree slices and plotted the number of stars per sample (global, blue and red MS) over the total number in Fig. 8. The three ratios show a decrease of the number of stars towards the direction of $\approx$ -90, 0, 90, 180°, where 0°is in the East direction, due to the lack of coverage of DECam photometric catalog (see Fig. 1), and maintain otherwise consistent values as a function of angle around the cluster. DECam data do not seem to support the presence of asymmetries in the distribution of all stars, and stars of the bMS and rMS sub-populations, until a distance of $\approx 140'$ from ω Cen center.

Model fits to the global stellar density profiles (see details in Appendix A) suggest the presence of potential escaper (PE) stars, distributed symmetrically around the cluster and forming a stellar halo (these stars are energetically unbound but still physically trapped within the cluster). Moreover, our dataset does not confirm the stellar over-densities identified with VST at 1 and 1.2° from the center, and possibly connected to the tidal tails (Marconi et al. 2014).

4.2. *Ellipticity*

We also used the combined ACS+WFI+DECam photometric catalog to investigate the presence of asymmetries in ω Cen by computing its ellipticity profile. The stars were selected in magnitude, as previously done to construct the global density profile for ω Cen, to ensure a similar completeness level of the dataset across its spatial extent. To verify that the fingerprints of the observed fields (ACS, WFI, and DECam, see Fig. 1) are not imposing a biased geometry on the distribution of the stars, we looked at the local density (computed by considering the location of the 30th nearest neighbor for each star) for stars in the cluster. Then

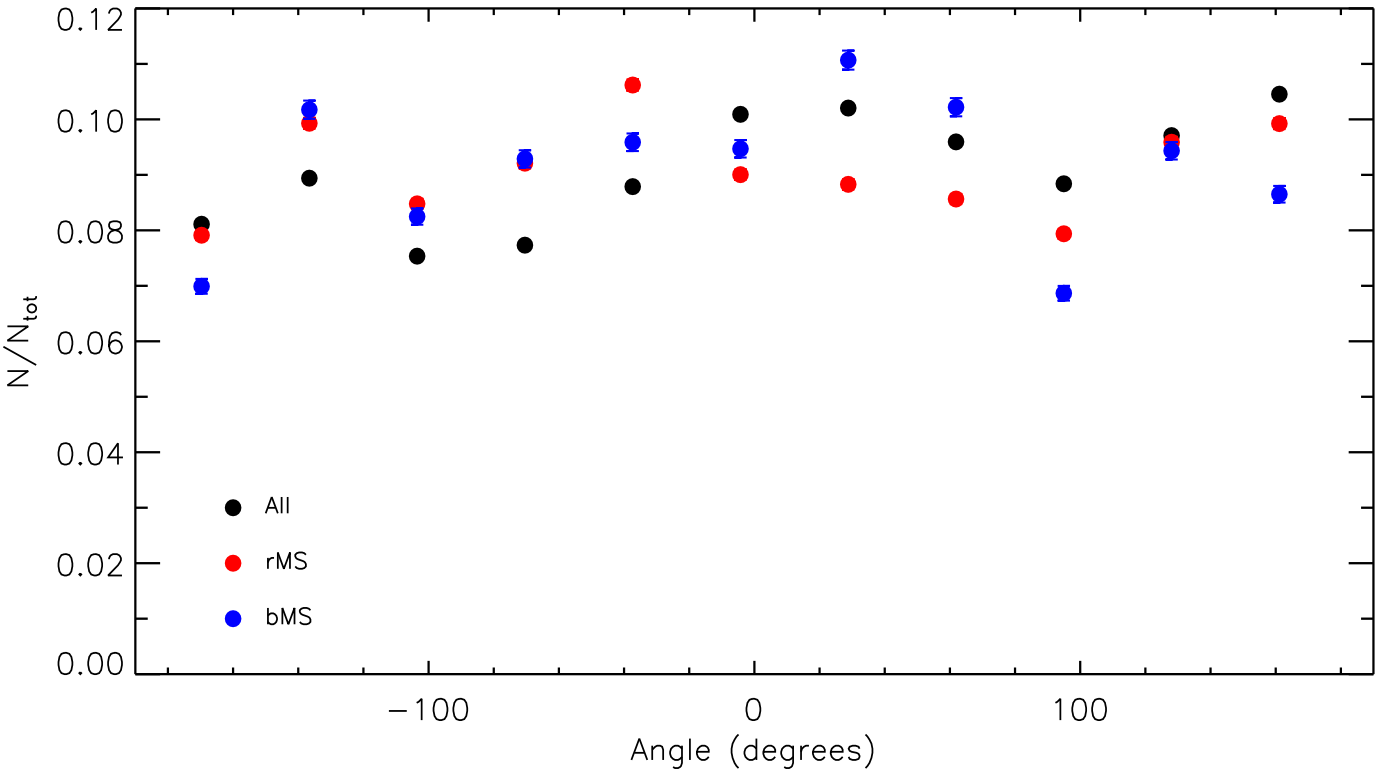

Figure 8. Normalized number of stars for the global (black points), bMS (blue) and rMS (red) samples of stars as a function of angle around ω Cen, with zero in the East direction. Error bars are shown but are either the same size or smaller then the symbols displayed.

we calculated the average of this quantity in each cell of a grid, and we interpolated the result to obtain a smooth function. The grid used in this case has cells with width of $\sim 0.24'$. The logarithm of this density, normalized with respect to its peak value is shown in Fig. 9. The isodensity contours correspond to values -4.5,-4.25,-4,-3.5,-3,-2.5,-2,-1.75,-1.5,-1.25,-1,-0.75,-0.5 of this function.

We then computed the ellipticity of ω Cen by determining the parameters of the ellipse which provides a best fit to each considered isodensity contour. Combining ACS data for the center of ω Cen to WFI and DECam data for more external regions, allowed us to study the variation of the ellipticity as a function of the cluster semi-major axis from $\sim 2'$ to $\sim 30'$. Fig. 10 shows the ellipticity, ε, as a function of the cluster semi-major axis, a, with $\varepsilon = 1 - b/a$ (where b is the semi-minor axis of the ellipse). This figure clearly shows that ω Cen is flattened, with average $\varepsilon \sim 0.10$, and that the ellipticity increases from the cluster center up to a maximum of ~ 0.16 at a radial distance of $\sim 8'$, then it is approximately constant until $\sim 15'$, and decreases again to ~ 0.05 at $\sim 30'$. Fig. 10 also shows the ellipticity profiles of ω Cen calculated by Geyer et al. (1983) based on photographic plate photometry and by Pancino et al. (2003) by using photometry of RGB stars: they both agree with the one presented here, even though the samples of stars used to compute them are different. In particular, the profile by Pancino et al. (2003) shows a remarkable agreement between ~ 2 and $10'$, and the one by Geyer et al. (1983) beyond $\sim 7'$.

5. THE RED-GIANT BRANCH STARS

The bMS has its counterpart in one of the RGB branches of ω Cen, possibly at a metallicity intermediate with respect to the range observed in the cluster. However, even very accurate HST photometry does not clearly show which RGB the bMS connects to (for more details on the correspondence between the cluster multiple MSs and SGBs and RGBs see Bellini et al. 2017a, Fig. 11). Moreover, it is not possible to separate the different intermediate RGBs without the information on the chemical composition of each star. For regions of the cluster until $\approx 25'$, low- and high-resolution spectroscopy is available for $\approx 1,000$ RGBs. For the outskirts of the cluster, no chemical information is available for a statistical significant number of RGB stars covering the entire cluster metallicity range (Da Costa & Coleman 2008). Thus we decided to investigate the spatial distribution of the brightest RGB stars by dividing them in metallicity groups according to their photometric $u-i$ color.

We selected 8,748 stars brighter than $i = 16$ mag and along the RGB in the DECam i, $u-i$ CMD. We then selected only stars with a Gaia proper motion measurement such that

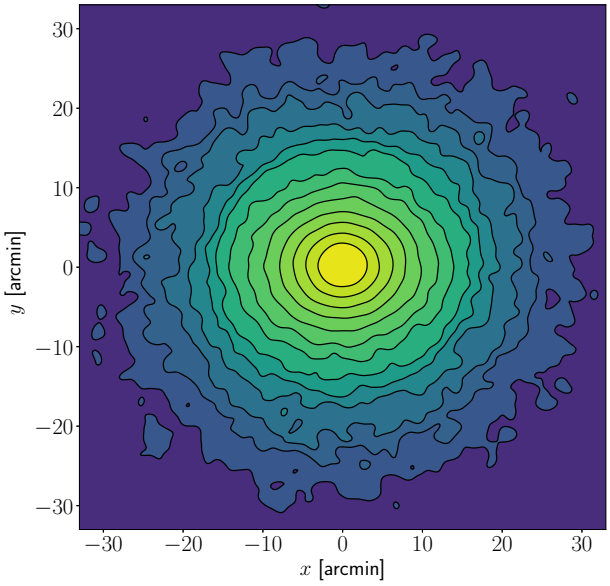

Figure 9. Surface density map and contours for ω Cen. Stars with $17 < r < 19$ mag are considered and the average of the local densities of stars is calculated for each cell of a grid and results are interpolated to obtain a smooth function. The logarithm of the density is normalized to its peak value and the plot shows contours corresponding to values of -4.5,-4.25,-4,-3.5,-3,-2.5,-2,-1.75,-1.5,-1.25,-1,-0.75,-0.5 of this function.

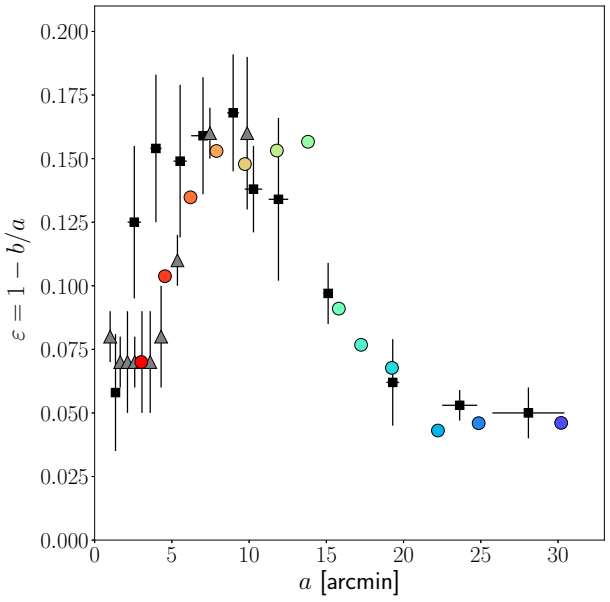

Figure 10. Ellipticity profile ε as a function of the semi-major axis a of the ellipses. Each point corresponds to one of the contour levels shown in Fig. 9, and is obtained by considering the parameters of its best-fit ellipse. The black squares report the ellipticity as estimated by Geyer et al. (1983), with error bars and horizontal bars marking the range of data considered; the grey triangles reproduce the profile calculated by Pancino et al. (2003), with error bars.

$-6.0 < \mu_\alpha < 0$ and $-10 < \mu_\delta < -3.5$ mas/yr, obtaining a sample of 4,525 RGBs. To divide the RGB in different metallicity groups, we selected stars starting from four ridge lines following the RGB from the bluest to the reddest color. The bluest ridge line selects the most MP RGB stars in ω Cen, according to spectroscopy. These stars, which correspond to the rMS stellar sub-population (see Bellini et al. 2017a), are the most abundant in the cluster, and we established them as the metallicity reference group. We then selected the faintest and reddest RGB, the RGB-a or ω3 branch, which constitutes the most MR sub-population of the cluster based on spectroscopic data (Pancino et al. 2000, 2007). The ω3 branch is well-separated from the other RGBs in the $i,\ u-i$ CMD, where the temperature sensitivity is larger (see Fig. 11). We also selected stars between the ω3 branch and the MP sub-population as representative of the ω Cen metal-intermediate sub-populations, and divided them in two groups, metal-intermediate 1 (MI1) and 2 (MI2).

The approach used to select RGB stars with different metallicities is similar to the method used by CA17: four ridge lines are drawn following the MP, MI1, MI2 and MR RGBs on the $i,\ u-i$ CMD, and stars are selected to be 0.50, 0.27, 0.37, 0.85 mag fainter and brighter than these ridge lines, respectively. Fig. 11 shows the selected sample of MP (blue dots), MI1 (green), MI2 (magenta), and MR (red) stars and the adopted ridge lines plotted on the $i,\ u-i$ CMD. The four samples of cluster stars have approximately the same completeness since they are selected in the same magnitude range, $16 \lesssim i \lesssim 12.5$, and include 2,076, 941, 640, and 111 objects, respectively. Note that the aim of this analysis is to divide stars in metallicity groups to study their spatial distribution and compare it to the spatial distribution of the rMS and bMS stellar sub-populations, not to identify and separate all the different sub-populations along ω Cen RGB. Moreover, we are interested in investigating the spatial distribution of these stars as a function of metallicity, and not in determining absolute star counts and ratios of the different sub-populations.

Calamida et al. (2009) provided a photometric metallicity distribution based on $\sim 4,000$ ω Cen RGB stars, by using the theoretical, empirical and semi-empirical calibrations of the Strömgren metallicity index m_1 (and the reddening free $[m]$) presented in Calamida et al. (2007). The average photometric metallicity of the main peak of the distribution was found to be $[Fe/H]_{phot} = -1.73 \pm 0.08$, in very good agreement with high-resolution spectroscopy, which found the main peak at $[Fe/H] \sim -1.75$ (Johnson & Pilachowski 2010). We assumed $[Fe/H]_{phot} \sim -1.73$ as the average metallicity of the MP group and estimated the metallicity of the RGB stars belonging to the four groups by using their $u-i$ color distance from the MP ridge line, $\Delta(u-i)$. The photometric metallicity

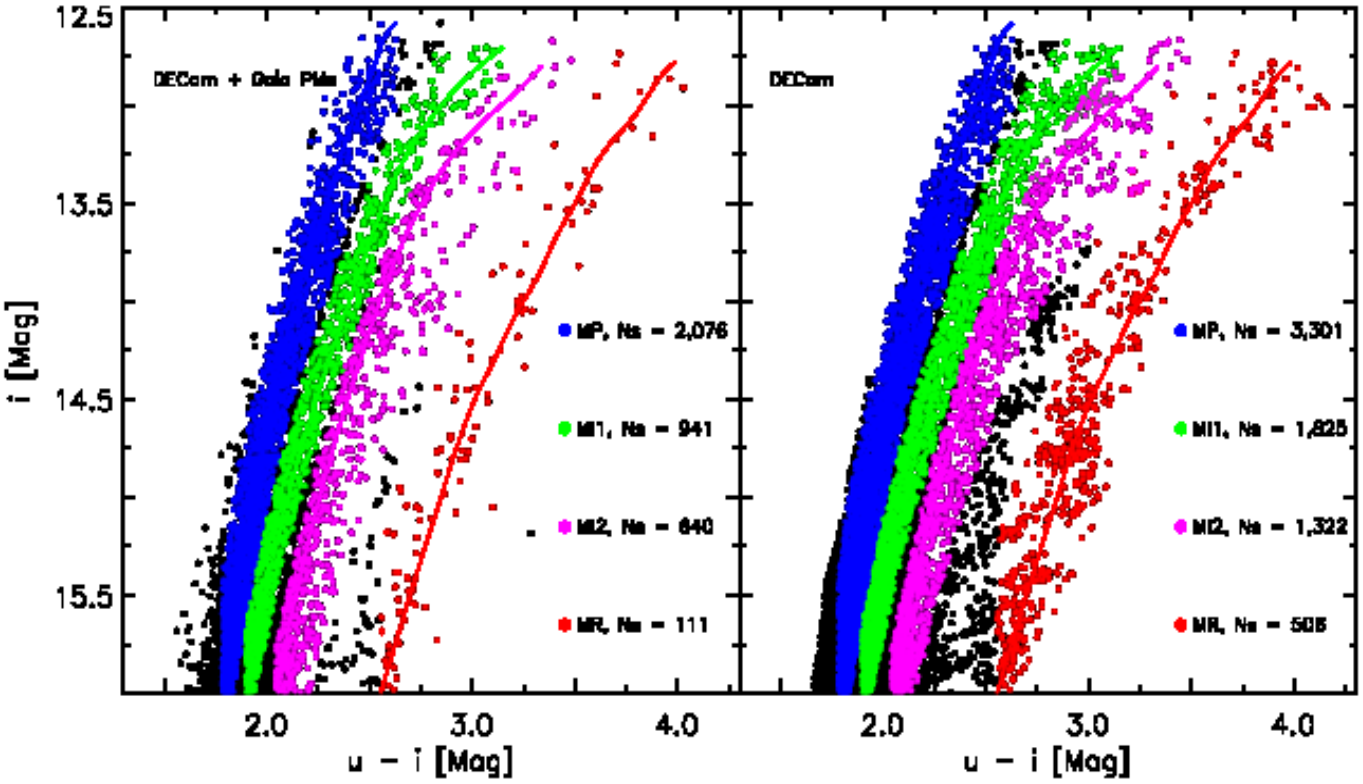

Figure 11. Left: DECam i, $u-i$ CMD of proper-motion selected ω Cen RGB stars. The four groups of candidate MP, MI1, MI2 and MR stars, and the ridge lines used to select them, are indicated in blue, green, magenta and red, respectively. The number of stars for each group is also provided. Right: Same CMD for stars not selected with proper motions.

is estimated as:

$$[\mathrm{Fe/H}]_{\mathrm{phot}} = -1.73 - \Delta(u-i) \quad (1)$$

for the MI1, MI2, and MR RGB stars. For the MP RGB stars the metallicity is estimated as:

$$[\mathrm{Fe/H}]_{\mathrm{phot}} = -1.73 - 2 \times \Delta(u-i) \quad (2)$$

where

$$\Delta(u-i) = (u-i)_i - (u-i)_{MP} \quad (3)$$

We used different criteria to estimate the metallicity of the MP group because this sub-population includes $\sim 70\%$ of the cluster stars and its metallicity peak has a dispersion a factor of 2 larger than the peaks of the other sub-populations in the photometric metallicity distribution (see Table 13 and Fig. 17 in Calamida et al. 2009). Note that we are only interested here in separating RGB stars with different metal content to study their spatial distribution, not in accurately measuring the metallicity (or iron abundance) of the individual stars. The photometric metallicity distribution obtained with this method is plotted in Fig. 12 as a dotted line. This figure also shows the metallicity distribution for 855 ω Cen RGBs (solid line) based on high-resolution spectroscopic measurements by Johnson & Pilachowski (2010). The two distributions agree quite well, and extend for more than 1 dex, from $[\mathrm{Fe/H}] \sim -2.2$ until ~ -0.2. Both the photometric and spectroscopic distributions have a main peak around $[\mathrm{Fe/H}] \sim -1.7$, a secondary peak around $[\mathrm{Fe/H}] \sim -1.45$, and a shoulder and tail up to higher metallicities.

We then calculated the difference between the photometric metallicity of the RGB stars of all groups and the reference value $[\mathrm{Fe/H}]_{\mathrm{phot}} = -1.73$. We interpolated the metallicity values of all stars by using an inverse distance algorithm and created a 2-D map of the RGB metallicity across ω Cen as a function of position, which is shown in the top panel of Fig. 13. This metallicity map shows a clear East-West asymmetry, with more metal-rich stars in the Eastern half of the cluster. Moreover, the more metal-poor stars seems to be offset from the geometrical center of the cluster. However, the current metallicity map is based only on RGB stars with a Gaia proper motion measurement; this selection introduces a bias in the spatial distribution since Gaia does not cover ω Cen uniformly, in particular towards the cluster center, due to the choice of the scanning law and crowding effects. This bias could cause the observed asymmetry and the center shift of the more metal-poor stars in the RGB metallicity map. Therefore, to have a better uniformly distributed sample of

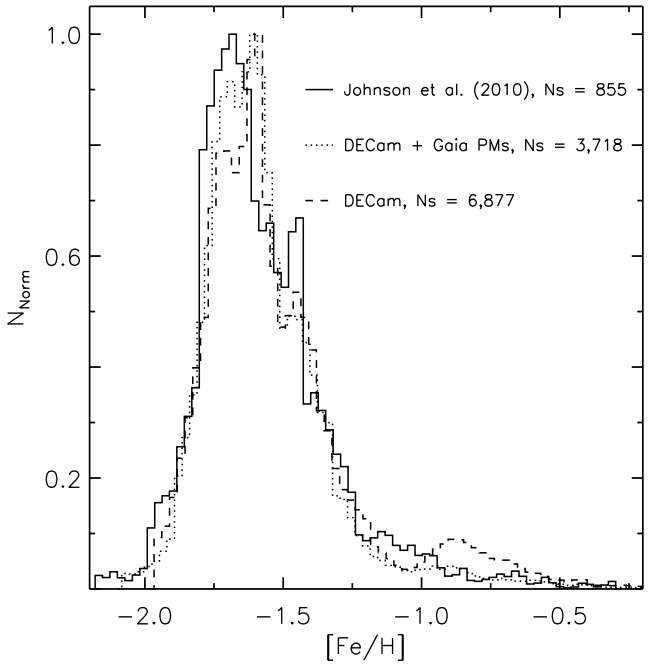

Figure 12. Metallicity distribution obtained by using the $u-i$ color of RGB stars selected from DECam i, $u-i$ CMD and Gaia proper motions (dotted line), selected by only using the $u-i$ color (dashed), and the high-resolution spectroscopic metallicity distribution (solid).

RGB stars, we selected them by using the i, $u-i$ CMD of ω Cen members without selecting stars with a proper motion measurement in Gaia. We used the same ridge lines and delta magnitude values as before and selected four new samples of RGB stars. The new selection includes 3,301, 1,825, 1,322, and 506 stars for the MP, MI1, MI2 and MR groups, respectively. The stars are shown on the i, $u-i$ CMD in the right panel of Fig. 11. We estimated the photometric metallicity for the four groups of stars and the obtained global metallicity distribution is shown in Fig. 12 as a dashed line. This distribution is in very good agreement with the previous photometric (dotted) and with the spectroscopic (solid) metallicity distribution. However, a peak at higher metallicities, [Fe/H] ≈ -0.9, is visible in this distribution, and it might be due to a higher contamination of field stars in the color range of the MR RGB group (field stars are on average more metal-rich than cluster stars).

The metallicity map based on this larger sample of RGB stars is shown in the middle panel of Fig. 13. This map allows us to draw a few qualitative conclusions on the spatial distribution of cluster RGB stars:

- metal-poor and metal-rich RGB stars have different spatial distribution in ω Cen;

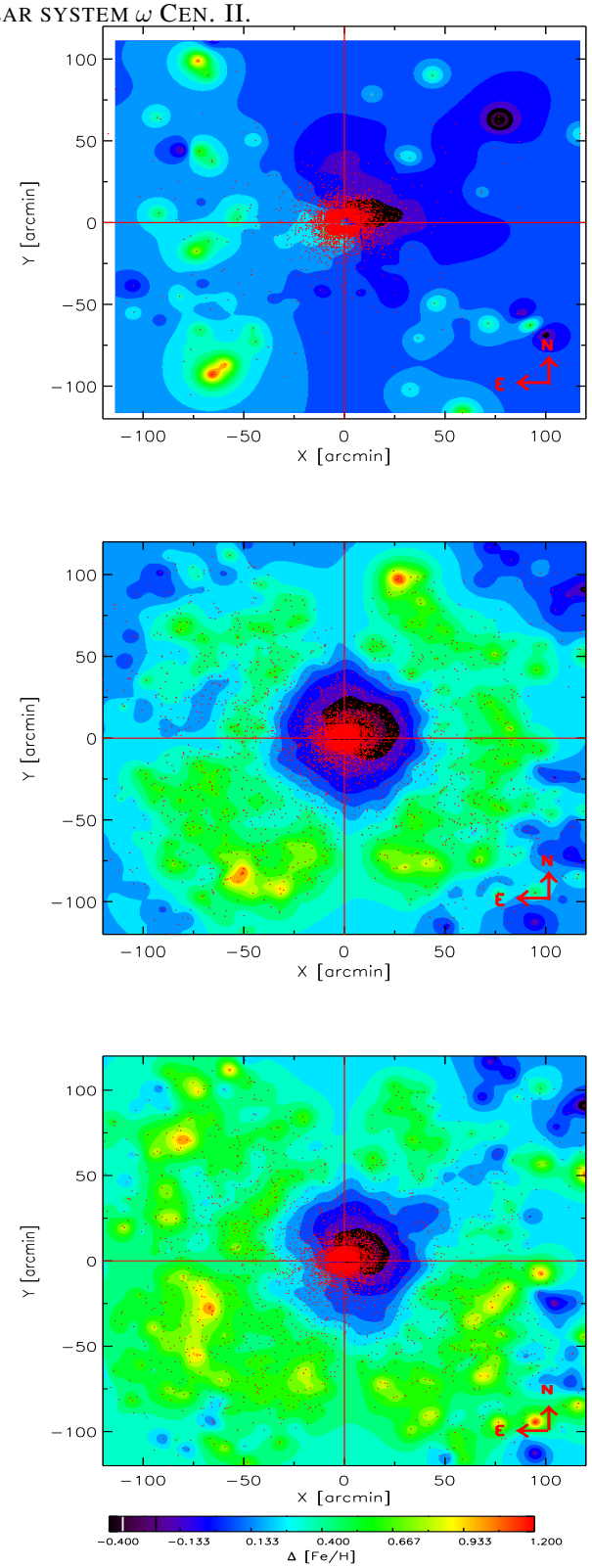

Figure 13. Metallicity maps for RGB stars selected from ω Cen i, $u-i$ CMD and Gaia proper motions (top panel), from the CMD only (middle), and excluding the most metal-rich stars (bottom). The selected RGB stars are over-plotted as red dots, and the North and East directions are labeled. We note that the tidal tails discovered by Ibata et al. (2019) are in the direction South East – North West, i.e. from the bottom left corner towards the top right corner of the plots presented here.

- the more metal-rich stars have a more extended spatial distribution compared to more metal-poor stars, i.e. they are more frequent in the outskirts of the cluster;
- the more metal-poor stars are more concentrated towards ω Cen center, and more metal-poor stars seem to be present in the Northern half of the cluster;
- the more metal-poor stars clearly show an offset from the geometrical center of the cluster.

Since metal-rich stars could be affected more by the field star contamination, we performed the same experiment by excluding the MR group from the RGB metallicity map. The result is shown in the bottom panel of Fig. 13: even by excluding the MR group, the more metal-rich RGBs are still more frequent in the outskirts of ω Cen, and the more metal-poor stars are off-center.

As a validation of our results we verified if reddening might affect them. ω Cen reddening map in Fig. 6 shows that there is a reddening increase towards the South-West quadrant of the cluster and a decrease in the North-West, with the dispersion of the extinction being less than 0.03 mag. An increase in the reddening would cause the RGB stars to seem redder, while a decrease would make them bluer, simulating higher or lower metallicities, respectively. If reddening is the culprit of the different spatial distribution of more metal-poor and more metal-rich stars, then the cluster metallicity map should resemble the reddening map, mostly in the outskirts of ω Cen. However, the two maps are quite different, with the metallicity map showing a more extended spatial distribution of the more metal-rich RGB stars in all four quadrants, while extinction substantially increases only in the cluster South-West quadrant. The more metal-poor RGB stars are more concentrated and more abundant in the Northern half of ω Cen. The North-South asymmetry and the center shift of the more metal-poor stars could then be partly due to the decrease of reddening in this area of the cluster.

To further investigate the role of reddening, we constructed a reddening-free color index as $[u-r] = (u-r) - 1.19 \times (g-i)$. To estimate the reddening ratio, $E(u-r)/E(g-i)$, we calculated the extinction coefficients for the *ugri* filters by using the Cardelli et al. (1989) reddening law and DECam filter transmission functions. We obtained $A_u = 1.70 \times A_V$, $A_g = 1.18 \times A_V$, $A_r = 0.84 \times A_V$, and $A_i = 0.63 \times A_V$, and $E(u-r)/E(g-i) = 1.19$. We then used the reddening-free $[u-r]$ color to separate RGB stars in the four groups, MP, MI1, MI2 and MR, instead of the reddening affected $u-i$ color. Note that extinction would move stars almost horizontally in the i, $u-i$ or i, $u-r$ CMDs, so we can neglect the reddening affecting the i magnitude for the purpose of selecting the groups of RGBs. The photometric metallicity was derived as before, by using a MP reference ridge line in the i, $[u-r]$ CMD and a reference metallicity of

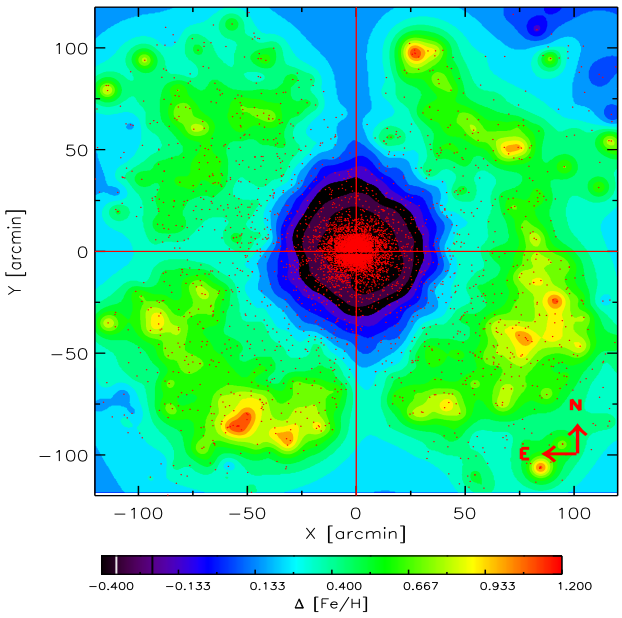

Figure 14. Metallicity maps as derived for RGB stars selected from ω Cen i, $[u-r]$ CMD. The selected RGB stars are over-plotted as red dots, and the North and East directions are labeled. We note that the tidal tails discovered by Ibata et al. (2019) are in the direction South East – North West, i.e. from the bottom left corner towards the top right corner of the plot presented here.

$[\mathrm{Fe/H}]_{\mathrm{phot}} = -1.73$. The reddening map based on this selection is shown in Fig. 14 and is in very good agreement with the map derived by selecting stars using the i, $u-i$ CMD. The more metal-poor RGB stars are more concentrated towards ω Cen center and the more metal-rich are more numerous in the outskirts. However, the more metal-poor RGBs seem to be less off-center in this metallicity map, even though the shift is still present. Therefore, differential extinction towards ω Cen cannot fully account for the different spatial distribution of the more metal-poor and more metal-rich stars.

To investigate further the different spatial distribution of stars at different metallicities, we also used another approach. We computed the local number density for each RGB of the four groups (MP, MI1, MI2, and MR) by determining which area includes the star and its 30 nearest neighbors. Then, we overlaid a grid on the top of the cluster and computed the number density within each cell by averaging the local number densities associated to the stars in the cell. We interpolated this number density with respect to the coordinates, x and y (by considering the centers of the cells as their x, y coordinates) to obtain a surface density function. We considered the logarithm of this function to better explore the areas of low densities. Finally, we applied a Gaussian filtering to the number density logarithm to remove stochastic fluctuations and to smooth the result. By varying the width of the cells in the grid and the σ of the Gaussian filtering, a slightly differ-

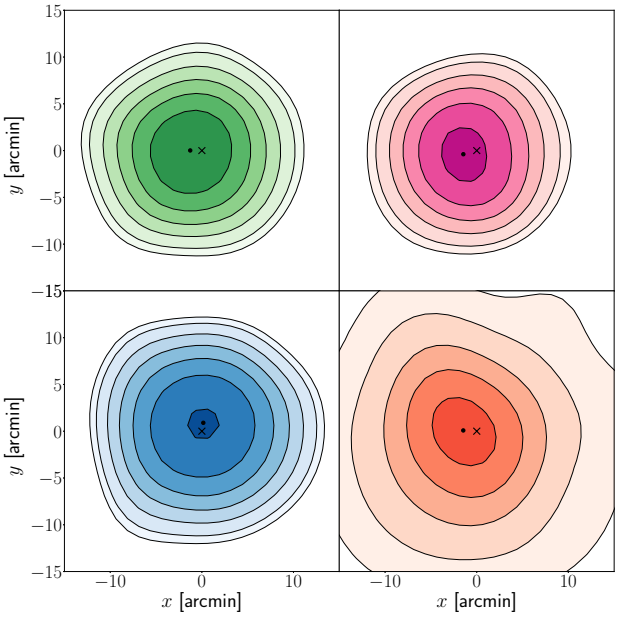

Figure 15. Isodensity maps of the four samples of RGB stars considered here. From the bottom left panel and proceeding clockwise: MP (blue), MI1 (green), MI2 (magenta), and MR (red) RGB sample, respectively. The cross marks the geometrical center of ω Cen and the center of each distribution of stars is marked in with a dot.

ent result is obtained for this function. However, the relative properties of the distributions of the four groups of RGB stars do not depend on how we computed them, and thus we decided to consider a grid with cell width $\sim 1.23'$ and $\sigma = 3'$ for the Gaussian filtering.

Fig. 15 shows the distribution of RGB stars in the four metallicity groups by using the chosen (logarithmic) surface density function as described above. This figure shows that the distribution of the MR sample (red) is more extended, and the distributions of the MP sample (blue), MI1 (green) and MI2 (magenta) is more concentrated, confirming the previous result. Moreover, the isodensity map of the MP and MI1 groups (blue and green contours in Figs. 15 and 16, $[Fe/H]_{phot} \lesssim -1.4$) show a slight East-West elongation, following ω Cen major axis direction, indicative of the cluster ellipticity. On the other hand, the isodensity maps of the MI2 and MR groups (magenta and red contours in Figs. 15 and 16, $[Fe/H]_{phot} \gtrsim -1.4$) are more elongated in the North-East to South-West direction.

The relative distribution of the samples can be better explored by looking at the three panels of Fig. 16, where the contours obtained from the density distributions of MI1 (solid green lines), MI2 (solid magenta), and MR (solid red) RGB stars are compared to those obtained for MP (blue dotted) stars. The centers of the distributions of the four samples do not exactly coincide with the geometrical center of the cluster (marked as a cross in the figure): the center of the distribution of the MP RGB stars (blue filled circle) is displaced in the North direction and the centers of the other distributions (filled triangles) in the South-East direction with respect to the center of ω Cen. The centers of the MI1, MI2, and MR distributions are shifted $\approx 2'$ from the center of the MP distribution and $\approx 1.4'$ South-East of the cluster center, while the MP distribution is $\approx 1'$ offset in the North direction.

The isodensity maps and contours of Figs. 15 and 16 confirm that more metal-poor and more metal-rich RGB stars have different spatial distributions in ω Cen, and that stellar sub-populations with different metallicities have also different centroids compared to the geometrical center of the cluster.

5.1. *The red-giant branch star counts*

We also explored if the four groups of RGB stars show differences in the star counts across ω Cen. We counted the number of MP, MI1, MI2, and MR RGB stars in the four - NE, NW, SE, and SW - quadrants of the cluster. The number of stars for the four metallicity groups and the ratio of the number of MR, MI1, and MI2 stars over the MP stars are listed in Table 1. The MR to the MP star count ratios indicate that MR stars are slightly more abundant in the South-East quadrant of ω Cen, and the MI1 and MI2 to the MP star count ratios are larger in the Eastern half of the cluster (columns 2, 3, and 4 of Table 1). This evidence confirms the spatial distribution shift between more metal-poor and more metal-rich stars shown by the isodensity maps and contours. Regarding the star counts (last four columns of Table 1), the MP RGB stars seem to be more abundant in the Northern half of ω Cen, while the more metal-rich RGB stars (MI1, MI2, and MR) are more numerous in the Eastern half of the cluster. These findings confirm the results of CA17, obtained with a smaller sample of RGB stars, where a East-West asymmetry was observed for the distribution of MI stars and mildly for the MR stars.

5.2. *Comparison with the Literature*

We compareed our results with previous studies based on the photometry and spectroscopy of ω Cen RGB stars. The analysis of Jurcsik (1998), based on the chemical abundances of 369 RGB stars, found that the more metal-rich RGB stars, with $[Fe/H] \geq -1.25$, are segregated in the Southern half of ω Cen, while the more metal-poor, with $[Fe/H] \leq -1.75$, in the Northern half. Jurcsik (1998) also found that the centers of the more metal-poor and the more metal-rich stellar groups are offset by $\approx 6'$. The segregation of the more metal-rich RGB stars in the Southern half of the cluster was later confirmed by Hilker & Richtler (2000), based on the photometric metallicity of 1,448 stars, but they could not find any North-South asymmetry in the distribution of the more metal-poor RGB stars in ω Cen.

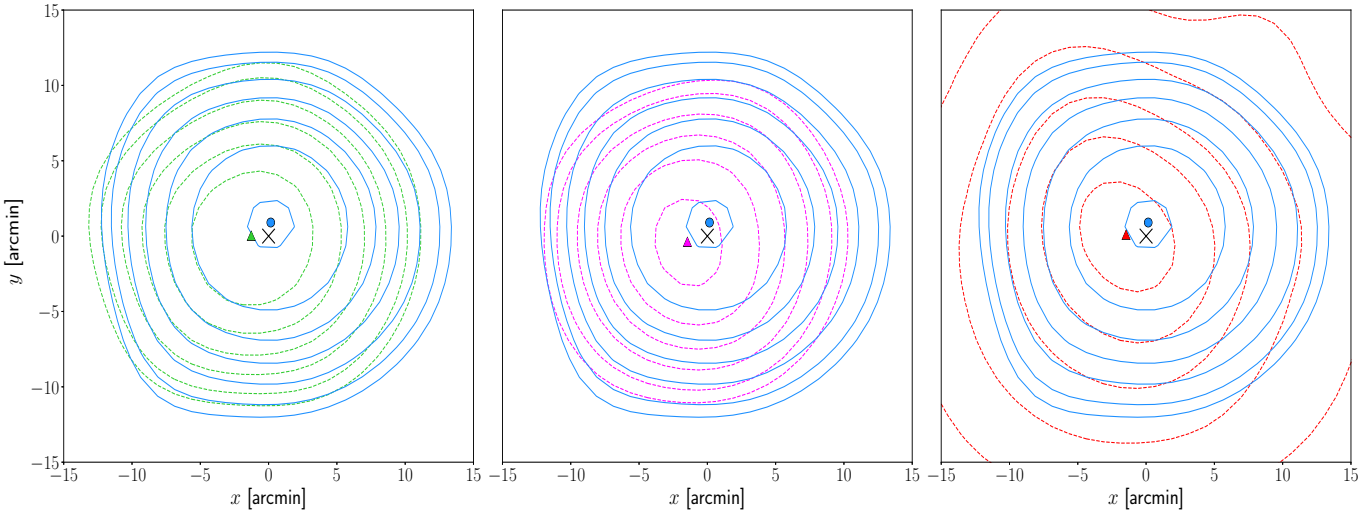

Figure 16. Comparison of isodensity contours for the four samples of RGB stars considered here. The panels show the contours obtained for the MI1 (left, green), the MI2 (middle, magenta), and the MR group (right, red) as compared to those obtained for the MP group (blue). The center of ω Cen is marked with a cross, while the centers of the MI1, MI2, and MR groups are marked with triangles and the center of the MP distribution with a circle.

Table 1. Number of metal-poor (MP), metal-intermediate (MI1, MI2), and metal-rich (MR) red-giant branch stars in the different quadrants of ω Cen and their ratios.

Quadrant	$N(MI1)/N(MP)$	$N(MI2)/N(MP)$	$N(MR)/N(MP)$	$N(MP)$	$N(MI1)$	$N(MI2)$	$N(MR)$
NW	0.45±0.03	0.28±0.02	0.13±0.01	867±29	395±20	244±16	112±11
SW	0.52±0.03	0.42±0.03	0.16±0.02	768±28	402±20	327±18	124±11
SE	0.62±0.04	0.51±0.03	0.18±0.02	749±27	466±22	381±19	135±12
NE	0.63±0.03	0.40±0.02	0.15±0.02	873±29	547±23	353±19	134±12

Pancino et al. (2003) used photometry for a field of view of $\sim 20' \times 20'$ across ω Cen to study the spatial distribution of $\sim 3,500$ RGB stars divided in three metallicity groups, MP, MI and MR. They found different spatial distributions, with the MP stars elongated in the East-West direction, i.e. along the cluster major axis, and the MI and MR elongated North-South in the internal regions, and East-West in the outskirts of the cluster (up to $\sim 20'$ from ω Cen center). Moreover, the MI group has a center located $\approx 1'$ South of the center of the MP group, while the MR group is centered North compared to the other two groups.

Our current data support a different spatial distribution of RGB stars in ω Cen as a function of metallicity and are in partial agreement with Jurcsik (1998): we find that MP RGB stars seem to be more abundant in the Northern half of ω Cen, as found by those authors, but that the more metal-rich RGBs (MI1, MI2, and MR) are more numerous in the East quadrant of the cluster, not in the South, with their centers shifted by $\approx 1.4'$ towards the South-East direction. We also found an offset between the centers of the MP and the more MR RGB stars, but it is a factor of three smaller that what found by Jurcsik (1998) ($2'$ vs $6'$). These differences could be due to a lack of statistics in the study from Jurcsik (1998) (369 as compared to our $\sim 7,000$ RGB stars) and to a different selection of the RGB star metallicity groups.

The results based on our data are in quite good agreement with the findings of Pancino et al. (2003): we see that the MP group of RGB stars follows the cluster spatial distribution, being mostly elongated in the East-West direction (see the bottom left panel of Fig. 15, and § 4.2 for the ellipticity estimate), and the most metal-rich RGBs in our study, the MI2 and MR groups, are elongated in the direction North-East to South-West. However, we found that the centroids of the more metal-rich RGBs (MI1, MI2 and MR) are $\approx 1.4'$ South-East of ω Cen center, while Pancino et al. (2003) found that the MI RGB group is $\approx 1'$ offset towards the South, but the MR group is $\approx 1'$ offset towards the North. This difference could be due to different statistics, completeness, and coverage of the photometric catalog, together with a different selection of the RGB metallicity groups.

6. DISCUSSION

The origin and formation history of ω Cen is still surrounded by mystery. ω Cen is one of the few GGCs that not

only shows light-element dispersions and anti-correlations, but also has a large spread in iron abundance and a dispersion of the heavy element content. Numerous photometric and spectroscopic studies in the last 50 years unveiled different properties of this cluster, which make it a unique object. However, a full understanding on how ω Cen formed and evolved is still missing. In this section, we analyze how the new results presented in this work can improve our understanding of the origin of ω Cen.

CA17 already showed that bMS stars are more centrally concentrated compared to rMS stars up to a distance of $\approx 25'$, while they are more numerous compared to rMS stars at larger radial distances, based on DECam data. In the current work, we confirmed these findings and, thanks to the larger field of view observed with DECam, we found that the number of bMS stars further increases in the outskirts of ω Cen, with bMS stars outnumbering rMS stars at distances larger than $\sim 100'$ from the cluster center. We then used multi-band DECam photometry to divide RGB stars in four groups according to their photometric metallicity, as estimated by using their $u-i$ color. We found that the more metal-rich RGB stars show a more extended spatial distribution compared to the more metal-poor RGBs; bMS stars should also be more metal-rich compared to rMS stars according to the available spectroscopy. The above evidence makes ω Cen one of the few stellar systems known where more metal-rich stars have a more extended spatial distribution compared to more metal-poor stars.

In nearby dwarf spheroidal galaxies such as Carina, Sculptor, Fornax, and in satellite dwarf galaxies of M 31, the more metal-rich stellar sub-populations are centrally concentrated (Monelli et al. 2003; del Pino et al. 2013; Fabrizio et al. 2015; Ho et al. 2015; Martínez-Vázquez et al. 2016). The same behavior is observed in Terzan 5, a bulge GGC with a significant spread in iron abundance. The metal-rich sub-population in this cluster is more centrally concentrated compared to the metal-poor one (Ferraro et al. 2016). However, in M 22 and NGC 1851, the more metal-rich stellar sub-population shows a more extended spatial distribution compared to the more metal-poor sub-population (Lee 2015; Yong & Grundahl 2008; Carretta et al. 2010, 2011). A merger scenario was proposed to explain the origin of M 22 and NGC 1851.

In the past, several authors have suggested that ω Cen could also be the result of the merger of two or more clusters. Norris et al. (1997) and Smith et al. (2000) for example, proposed the "merger within a fragment" scenario (already advanced by Searle in the 70's, Searle & Zinn 1978), where multiple sub-structures with different chemical abundances evolve in the same parent cloud and gravitational field, in slightly different time scales, to form a dwarf galaxy with a globular cluster system. The most external clusters would later be accreted onto the Galaxy, while the most internal ones would fall on the center of the dwarf. The remnant of the dwarf nucleus merged with the small clusters would then also be accreted by the Galaxy and form a chemically complex massive GGC, such as ω Cen.

Makino et al. (1991) and Thurl & Johnston (2002) produced N-body simulations of globular clusters merging and showed that the probability of a merging happening in the halo of the Galaxy is very low in a time interval less than 10 Gyr. However, encounters (and merging) of globular clusters are more probable in dwarf galaxies. This process could have happened in the Sagittarius dwarf spheroidal galaxy, currently accreting onto the Galaxy, and formed the massive central cluster M 54, suggested to be a nuclear stars cluster by Alfaro-Cuello et al. (2019). In their recent work, Alfaro-Cuello et al. (2019) showed that the oldest more metal-poor sub-population in M 54 could result from the merging of two clusters: its stars are more centrally concentrated compared to the metal-intermediate stars, that could belong to the Sagittarius dwarf. A youngest more metal-rich sub-population was also identified and is more centrally concentrated compared to the metal-poor and metal-intermediate stars, and could have formed in situ.

Other studies provided theoretical simulations of globular cluster merging in a dwarf galaxy environment to explain the origin of clusters with light- and heavy-element abundance dispersions (Amaro-Seoane et al. 2013; Gavagnin et al. 2016; Pasquato & Chung 2016). The clusters resulting from the merger would then be accreted by the Galaxy after their host dwarf was disrupted. Amaro-Seoane et al. (2013) described globular clusters in neighbouring galaxies as a product of mergers, by means of dedicated numerical simulations with different initial conditions. In some cases, they found that more metal-rich stars were more concentrated in the centre of the cluster and also dominated in the outer parts of the system, which is qualitatively similar to what we see here for omega Cen. However, they pointed out that this is due to the specific choice of parameters describing the structure of the initial clusters. Bekki & Tsujimoto (2016) simulated the formation of globular cluster merging in dwarf galaxies orbiting the Galaxy, by assuming different chemical evolution models. According to the mass of the dwarf, its chemical composition, the masses of the clusters and their position in the dwarf, the merging can produce GGCs with different light-element dispersion, or with different light- and heavy-element dispersions. Moreover, some dwarf field stars could also be accreted by the merging clusters and further increase the chemical abundance anomalies of the GGC. The accretion of the dwarf field stars was suggested, in particular, to explain the origin of the anomalous RGB in ω Cen, i.e. the ω3 or RGB-a branch, which is the most metal-rich substellar population in the cluster, according to spectroscopy.

ω Cen could also be the remnant of the nucleus of such a dwarf galaxy that has been accreted onto the Galaxy.

In support of the merger scenario for the origin of ω Cen is the different spatial distribution of RGB stars at different metallicities and of the bMS and rMS stellar sub-populations. The more metal-rich RGB stars are more concentrated in the center of ω Cen, and show a more extended spatial distribution compared to the more metal-poor ones in the outskirts of the cluster. In a similar way, the bMS stars are more concentrated in the center of ω Cen and have a more extended distribution compared to the rMS stars at distances larger than $\sim 20'$ from the center. The currently available photometric and spectroscopic data show that bMS stars are slightly more metal-rich compared to rMS stars, and possibly more helium-enhanced. However, if the metal-rich RGB and the bMS stars were only the result of self-enrichment in ω Cen, these sub-populations should be more concentrated compared to the rest of the cluster stars. Dwarf galaxies in the Local Group and the few GGCs with a measurable metallicity spread that have been studied so far, show more metal-rich stars concentrated towards the center compared to more metal-poor stars, and no extended spatial distribution of these stars was observed in the outskirts of these systems.

However, as shown by multiple spectroscopic and photometric studies including this work, ω Cen shows a large metallicity spread, with a main peak at $\sim$ -1.7, a few secondary peaks and a tail up to $\sim$ -0.5. This evidence could indicate that one of the systems that merged to form ω Cen underwent some level of self-enrichment. This situation is indeed observed for M 54, which has a broad metallicity distribution and is considered the remnant of the nucleus of the Sagittarius dwarf galaxy in the process of accreting onto the Milky Way (Ibata et al. 1997; Alfaro-Cuello et al. 2019).

Another indication of a possible merger is the different location of the centers of the RGB stars spatial distributions: the distribution of the more metal-rich RGB stars shows a peak $\approx 1.4'$ offset from the cluster center, while the distribution of the more metal-poor stars is $\approx 1'$ off-center towards the North. The shift in the peaks of the RGB sub-population distributions was already observed by Jurcsik (1998) and Pancino et al. (2003), but the peaks had different shifts.

As a result of a merger, ω Cen could be flattened. And indeed, our ACS+WFI+DECam data show that ω Cen has an average ellipticity $\varepsilon \sim 0.10$, with a maximum value of ~ 0.15 between 8 and $15'$ from the cluster center. This result provides further evidence in support of this possible origin for ω Cen, but we point out that rotation or the effect of the external Galactic tidal field could also be responsible for the observed morphology, and we plan to investigate this further in the future.

If ω Cen is the result of a merger, the different stellar sub-populations should also show different kinematical properties if the system is not relaxed yet. Note that the relaxation time at the half-mass radius for ω Cen is $\gtrsim$ 12 Gyr (van de Ven et al. 2006), and signatures of the merger should then be observable in the cluster. Spectroscopy for a few hundreds of RGB and SGB stars is available for the more internal regions of ω Cen ($r \lesssim 30'$) and radial velocities were measured.

Norris et al. (1997) claimed that ω Cen sub-populations have different kinematical properties, and Ferraro et al. (2002) showed that the proper-motion centroid for the metal-rich stars is offset from the centroid of the metal-poor stars in ω Cen. On the basis of these findings, they suggested that the most metal-rich stars in ω Cen, i.e. the ω3 or RGB-a branch, formed in an independent stellar system that was later accreted by the cluster. These results were not confirmed by Bellini et al. (2009), who found a similar centroid for the proper motions of different populations when using a different set of ground-based data. Moreover, Pancino et al. (2007) and Sollima et al. (2009) found that metal-poor and metal-rich stars in ω Cen do not present any significant radial velocity offset. However, a study of radial velocities of ω Cen SGB stars from Sollima et al. (2005b), showed that the most metal-rich SGB stars, belonging to the SGB-a, i.e. the continuation of the RGB-a, show a larger velocity dispersion compared to the other SGBs, and suggested that these stars might have evolved in a different environment and were later accreted by ω Cen, supporting the merger scenario of ω Cen with accretion of field stars in a dwarf.

Unfortunately, radial velocities for SGB and RGB stars are not available yet in the outskirts of ω Cen, but the photometric study presented in this paper strongly supports the more metal-rich stars in the cluster having a different origin compared to the more metal-poor stars. This evidence also points to a merger formation scenario for ω Cen.

It is important to note that the merger scenario we propose for the origin of ω Cen does not exclude the possibility that this cluster has a surrounding stellar halo and/or tidal tails. Based on our new DECam photometry, we produced a stellar density profile from the core up to a distance of $140'$ from the centre of ω Cen. Model fits to the density profile (see details in Appendix A) suggest indeed that the cluster could be surrounded by a halo of PE stars. We plan to investigate this further by gathering kinematic data for stars in the outskirts of ω Cen, and also providing numerical simulations to determine if and which kind of progenitors could have merged to generate such a cluster and in which time-frame.

7. SUMMARY AND CONCLUSIONS

We presented DECam multi-band photometry of ω Cen for a FoV of $\approx 5^\circ \times 5^\circ$ across the cluster. The availability

of the u-band photometry allowed us to use a color-color-magnitude diagram to separate cluster and field stars down to $i \sim 22.5$ mag. We verified the efficiency of our method by using proper motions for the brighter stars, i$\leq$16 mag, obtained from Gaia DR2: our catalog has a residual contamination by field stars of $\lesssim 10\%$, while only $\sim 1\%$ of cluster stars are classified as field stars. The final DECam photometric catalog includes ≈ 0.5 millions cluster members, with photometry in 4 filters, namely *ugri*.

We matched DECam photometry with ACS and WFI photometry for the more internal regions of ω Cen. The combined catalog includes $\sim 1.8 \times 10^7$ cluster members and photometry in 11 filters. This unprecedented photometric catalog allowed us to observe the split along ω Cen MS and to analyze the spatial distribution of the blue and red MS across the entire cluster extension and beyond. We confirmed the evidence presented in CA17 that bMS stars are more centrally concentrated compared to stars belonging to the rMS up to a distance of $\approx 25'$. The frequency of bMS stars then steadily increases up to the tidal radius, with the ratio of bMS to rMS stars being ~ 0.85 and constant up to $\sim 100'$ from the cluster center. We used the extinction values towards ω Cen measured by Schlafly & Finkbeiner (2011) and found that our results are not affected by differential foreground reddening. Moreover, reddening would move stars from the blue to the red MS decreasing the ratio of bMS to rMS stars, further supporting our results that bMS stars have a more extended spatial distribution compared to rMS stars.

We also derived the global stellar density profile based on DECam photometry of ω Cen members for distances larger than $16'$, and WFI and ACS photometry for the more internal regions. This is the first time that ω Cen density profile is derived by using star counts of bright stars and fainter MS stars from 1 to $\sim 140'$ from the cluster center. We also investigated if the density profile varies in the direction of ω Cen tidal tails and along the opposite direction: these profiles are fully compatible, within uncertainties, with the cluster global density profile. To further ascertain this, we divided the cluster region in 15° slices, and calculated the ratio of normalized number of stars a function of the angle, finding no significant variations.

We also constructed stellar density profiles of the bMS and rMS stars, which suggest that the bMS stellar sub-populations is more extended compared to the rMS one in the outskirts of ω Cen, as determined also on the basis of the number ratio of bMs to rMS stars. We computed the density profile of the bMS and rMS stellar sub-populations along (and opposite to) the direction of the tidal tails, finding no significant difference with respect to the profiles shown in Fig. 7. Moreover, just like the total number of stars, the number of bMS and rMS stars do not show any significant variation as a function of angle.

We then computed the ellipticity profile of ω Cen by considering all stars from the combined ACS, WFI and DECam photometric catalog. The average ellipticity is ~ 0.10, and it increases from ~ 0.06 at $\sim 3'$ from the cluster center to ~ 0.16 at $\sim 10'$. It then decreases again at larger distances, reaching a value of ~ 0.05 at $\sim 30'$. At larger distances, the low density of stars and the non-uniform coverage of the field of view introduce geometrical biases and prevent us from measuring the real geometry of the system and from estimating reliable ellipticity values. Our results are in good agreement with Geyer et al. (1983) and with Pancino et al. (2003), within uncertainties.

We also studied the spatial distribution of RGB stars, divided in four metallicity groups, MP, MI1, MI2, and MR, according to their $u-i$ color. The metallicity map shows that more metal-rich stars have a more extended distribution compared to more metal-poor stars. The comparison between the metallicity and the reddening maps shows that extinction cannot fully account for this result.

The isodensity maps and contours of the four groups show that the more metal-poor stars, MP and MI1, follow the cluster elongation, while the more metal-rich, MI2 and MR, are elongated in the North-East – South-West direction. Moreover, the center of the MP group of stars is shifted $\approx 1'$ North of the geometrical center of ω Cen, while the centers of the MI1, MI2, and MR groups are shifted $\approx 1.4'$ South-East.

The star counts of the four groups of RGBs show that more metal-rich stars are more numerous in the Eastern half of the cluster, and the more metal-poor stars are more abundant in the Northern half. These results are in quite good agreement with previous studies; however, we show that the asymmetry in the distribution of more metal-rich and more metal-poor stars is in the East-West direction, with the center of the more metal-rich stars shifted South-East.

All this evidence supports a formation scenario where ω Cen is the result of a merger of different clusters, or of clusters and the nucleus of a dwarf galaxy, later accreted by the Galaxy, as discussed in § 6.

Spectroscopic data for a statistically significant number of stars in the outskirts of the cluster are now needed to confirm the formation scenario of ω Cen. The current wide-field photometry combined with abundances and radial velocity measurements for RGB stars in the outskirts of ω Cen will allow us to confirm the different spatial distributions of the stellar sub-populations and their different kinematical properties. Moreover, spectroscopy for a statistically significant number of stars along the MS of ω Cen is necessary to confirm that the bMS stars are more metal-rich than the rMS stars.

We also plan to carry out an investigation by means of dedicated numerical simulations, to determine if and which kind of progenitors could have merged to generate such a cluster;

we will aim at reproducing both the structure and the kinematics of the populations that it hosts. This would help us to clearly explain the puzzling properties of this peculiar stellar system, and to truly shed light on its origin.

Based on observations made with the Dark Energy Camera (DECam) on the 4m Blanco telescope (NOAO) collect during programs 2014A-0327, 2015A-0151, 2016A-0189, 2017A-0308, PIs: A. Calamida, A. Rest. This study was supported by the Space Telescope Science Institute, which is operated by AURA, Inc., under NASA contract NAS 5-26555. This work has made use of data from the European Space Agency (ESA) mission *Gaia* (https://www.cosmos.esa.int/gaia), processed by the *Gaia* Data Processing and Analysis Consortium (DPAC, https://www.cosmos.esa.int/web/gaia/dpac/consortium). Funding for the DPAC has been provided by national institutions, in particular the institutions participating in the *Gaia* Multilateral Agreement. AZ acknowledges support through a ESA Research Fellowship, and AMB acknowledges support by Sonderforschungsbereich SFB 881 "The MilkyWay System" (sub-project A8) Project-ID 138713538 of the German Research Foundation (DFG). We would like to thank the anonymous referee for helpful suggestions which led to an improved version of the paper.

Facility: *Blanco-4m* (DECam) *HST* (ACS), *MPG* (WFI), *Gaia*

APPENDIX

A. FIT TO THE CLUSTER STELLAR DENSITY PROFILES

In order to characterize more precisely the relative concentration of rMS and bMS stars and their extent in the cluster, we decided to carry out fits of dynamical models to the number density profiles of all cluster stars and of the bMS and rMS stars. We considered the isotropic, single-mass King (1966) and the non-rotating Wilson (1975) models because they have been extensively used in the literature to describe globular cluster profiles (thus allowing us to compare our results with previous studies in a meaningful way), and because, even though they are constructed based on simplifying hypotheses, they provide a good zeroth-order description of the structure of this class of stellar systems. In addition, we also considered LIMEPY models (Gieles & Zocchi 2015), and SPES models (Claydon et al. 2019).

The isotropic LIMEPY models are defined by two structural parameters: the concentration, W_0, and the truncation parameter, g, which describes the outermost slope of the models (small g values indicate an abrupt truncation, large g values a more shallow slope). We note that the King and non-rotating Wilson models can be obtained from this family of models by choosing $g = 1$ and $g = 2$, respectively. In this respect, the presence of the truncation parameter makes the LIMEPY models more flexible in reproducing the outermost parts of the observed density profiles, where the interaction with the external tidal field might play an important role in determining the cluster morphology.

The SPES models account for the presence of potential escaper (PE) stars, i.e. energetically unbound stars still spatially trapped within the cluster. They are defined by a distribution function composed of two parts, continuously and smoothly connected to each other, one describing the bound stars and the other representing the PEs. These models are defined by means of the usual concentration parameter, W_0, and two additional structural parameters, B and η. The B parameter is a constant used to connect the distribution function of the PEs to that of bound stars; its values range between 0 and 1, with $B = 1$ corresponding to a cluster without PEs. The parameter η is the velocity dispersion of PEs normalized with respect to the velocity scale of the models; its possible values also range from 0 (no PEs) to 1. Also in this case, it is possible to recover the King and non-rotating Wilson models with an appropriate choice of the values of the model parameters ($B = 1$ and $\eta = 0$ for the first, and $B = 1$ for any η for the second).

We show the best-fit profiles in Fig. 17: the top panel displays the number density obtained when considering all the stars (green filled circles), the central panel the profile obtained with only bMS stars (blue), and the bottom panel the profile obtained with the rMS stars (red). The LIMEPY, SPES, King and Wilson best-fit models are shown with dashed, solid, dotted and dashed-dotted lines, respectively. The fits of the LIMEPY, King and Wilson models were carried out on profiles extending up to a limiting radius of $50'$, and SPES models on profiles extending up to $80'$, to avoid the outermost points (dark and empty circles in all panels), which are not well-represented by these models, to drive the fits.

The best-fit models to the three groups of stars appear to be different, confirming the different concentration and extent of stellar sub-populations in ω Cen. The derived concentration parameters, half-mass and truncation radii for the best-fit models for the three profiles are listed in Table 2. We also list the values of the model parameters g (for LIMEPY, King and Wilson models), and B and η for the SPES models. For these models we also indicate the fraction of PEs present in the cluster, f_{PE}, calculated as the ratio of the total mass of PE to the total mass of the cluster.

The best-fit King and Wilson models for the bMS stellar density profile are slightly more concentrated (they have a larger concentration parameter, W_0) and more extended (larger truncation radius, r_t) compared to the rMS stellar density profile; a similar distribution for bMS and rMS stars is inferred when looking at the best-fit SPES models. The values of the truncation radii obtained with the LIMEPY models are very large: the best-fit value of g is large to accommodate the outermost part of the profile, and this drives the model extent to be very large. We note that the bMS profile starts to be flattened already at $\sim 35'$, and it is thus the profile with the largest estimated truncation radius.

The King models are unable to reproduce the stellar density distributions at large distances from the center, and their truncation radii are a severe underestimate of the edge of the cluster. The truncation radii obtained with the Wilson best-fit models are $\sim 100'$ for the global density profile, and ~ 150 and $\sim 120'$ for the bMS and rMS profiles, respectively (see Table 2). The Jacobi radius[2] for ω Cen was estimated by Balbinot & Gieles (2018) to be 161.71 pc, corresponding to $101.1'$, when assuming a distance to ω Cen of 5.5 kpc, a value in very good agreement with our estimate of the truncation radius obtained with the Wilson best-fit model to the global and rMS density profiles. This value is also quite close to the critical radius estimated with the best-fit SPES model for the global profile ($\sim 84'$), and for the rMS profile ($\sim 100'$), which represents the maximum radius for bound stars. It is worth noticing that the bMS profile has a smaller critical radius ($\sim 80'$) than the global and rMS profiles: bMS stars located at distances $> 35'$, where the profile flattens, are considered to be PEs, and consequently the derived critical radius is smaller in this case compared to those of the other profiles. The best-fit SPES model, indeed, provides the highest PE star fraction in mass (6%) for the bMS stellar sub-population.

Both the best-fit King and Wilson models, and partially also the LIMEPY models, fail to reproduce the outermost shape of the global stellar density profile, suggesting that the interaction with the Galactic tidal field, and the presence of PEs (Claydon et al. 2017) need to be taken into account to better describe the observations.

Our results agree quite well with the recent findings of de Boer et al. (2019), who used Gaia DR2 combined to HST photometry and surface density profiles from Trager et al. (1995) for the central parts to derive the density profiles of 81 GGCs. Gaia photometry is used down to $G = 20$ mag, which is about the TO level for the closest clusters. Most of these density profiles are therefore based on SGB and RGB stars. In the case of ω Cen, Gaia data are used starting from a distance of $17.5'$ from the cluster center, where the completeness should be $\sim$80% down to $G = 20$ mag, and the surface density profile from Trager et al. (1995) is used at smaller distances. This profile has been stitched and normalized to match Gaia star count data in the external regions of ω Cen. de Boer et al. (2019) also fit the same models considered in this work to the GGC profiles. The King and Wilson models do not properly fit the outermost regions of ω Cen ($r \gtrsim 60'$), and provide truncation radii of $\sim 48'$ and $\sim 78'$, and concentration parameters $W_0 = 6.25$ and 4.82, respectively. The best-fit LIMEPY model provides a truncation radius of $\sim 94'$ with $W_0 = 3.97$ and $g = 2.33$, and the best-fit SPES model provides a critical radius of $\sim 67'$ with $W_0 = 4.57$, $\log(1-B) = -2.83$ and $\eta = 0.25$. These values are a bit smaller but still in quite good agreement with the ones obtained with our fits, especially considering that we used a different sample of stars for the analysis. Summarizing, the SPES models provide the best fit to ω Cen stellar density profile and suggest that 2% of the mass of the cluster is due to PE stars in its surroundings.

To investigate for the presence of asymmetries in the stellar density distribution, we selected only stars in the North-West – South-East direction (tidal tail direction) and the opposite one, and produced a density profile considering all stars, bMS, and rMS stars in both directions. The six new profiles were also fit with the same four families of models introduced above, and the best-fit parameters are in very good agreement, within uncertainties, with the ones obtained for the global profiles, and show no significant difference in the distribution of stars along different directions.

[2] The Jacobi radius is defined as $r_J = R_G \left[M/(2M_G)\right]^{1/3}$, where R_G is the galactocentric distance of the cluster, and M and M_G are the masses of the cluster and of the Galaxy, respectively.

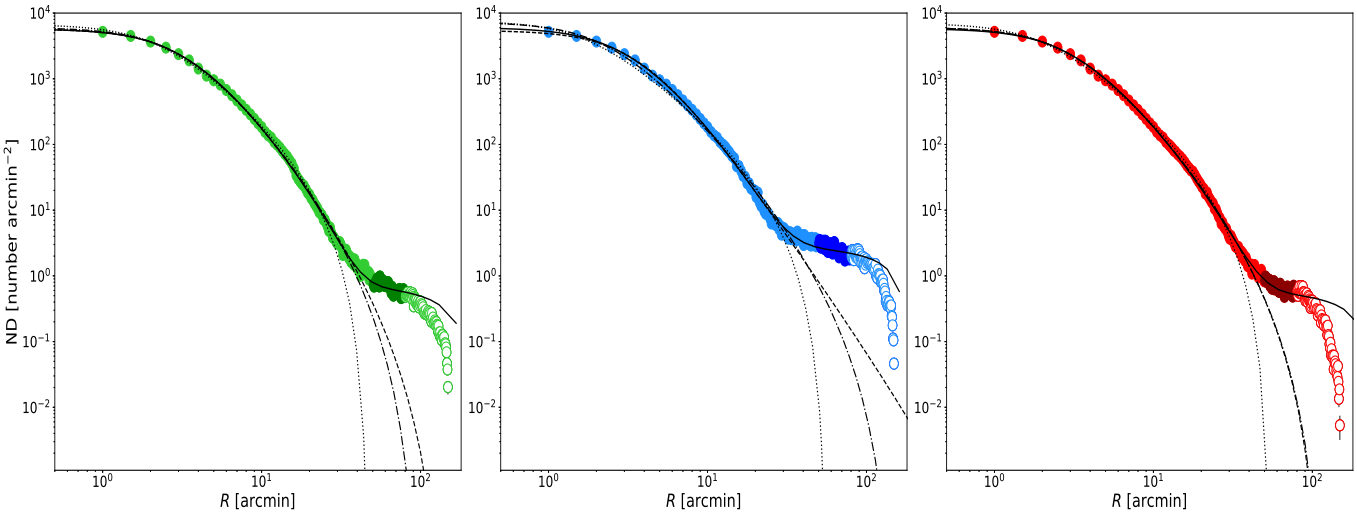

Figure 17. Number density profile for all selected cluster members (left panel) and for selected bMS and rMS stars (middle and right panels). Darker filled circles indicate the points excluded from the fit with LIMEPY, King and Wilson models, empty circles those excluded only from the SPES model fit. Dotted, dashed, dot-dashed and solid line reproduce the best-fit profiles of King, Wilson, LIMEPY and SPES models, respectively.

Table 2. Parameters of best-fit for the considered models, for each profile, as indicated in the first column. The first part of the table lists the best-fit parameters obtained for the LIMEPY models (Gieles & Zocchi 2015), and the third and fourth part the ones derived for King (1966) and non-rotating Wilson (1975) models: the concentration parameter W_0, the half-mass radius r_h (given both in pc and in arcmin), the truncation radius r_t (given both in pc and in arcmin), and the truncation parameter g; we recall that King and Wilson models can be obtained by calculating LIMEPY models with $g = 1$ and $g = 2$ respectively. The second part of the table lists the best-fit parameters obtained for the SPES models (Claydon et al. 2019): the concentration parameter W_0, the half-mass radius r_h (given both in pc and in arcmin), the critical radius r_{crit} (given both in pc and in arcmin), the model parameters B and η, and the fraction of the cluster in potential escapers, f_{PE}.

Profile	W_0	r_h (pc)	r_h (arcmin)	r_t (pc)	r_t (arcmin)	g	$\log(1-B)$	η	f_{PE}
				LIMEPY model					
All	$4.87 \pm^{0.26}_{0.37}$	$9.29 \pm^{0.11}_{0.12}$	6.39	215.81	148.33	$2.33 \pm^{0.21}_{0.16}$			
bMS	$3.95 \pm^{0.36}_{0.15}$	$9.58 \pm^{0.10}_{0.11}$	6.59	2766.00	1806.24	$2.90 \pm^{0.06}_{0.10}$			
rMS	$5.61 \pm^{0.15}_{0.17}$	$9.70 \pm^{0.12}_{0.12}$	6.72	171.09	117.61	$1.99 \pm^{0.12}_{0.11}$			
				SPES model					
All	$5.06 \pm^{0.10}_{0.08}$	$9.33 \pm^{0.14}_{0.15}$	6.41	121.82	83.75		$-3.28 \pm^{0.33}_{0.24}$	$0.78 \pm^{0.15}_{0.17}$	0.02
bMS	$5.09 \pm^{0.04}_{0.06}$	$9.52 \pm^{0.18}_{0.15}$	6.54	117.02	80.45		$-2.95 \pm^{0.08}_{0.05}$	$0.95 \pm^{0.04}_{0.06}$	0.06
rMS	$5.37 \pm^{0.09}_{0.10}$	$9.81 \pm^{0.15}_{0.15}$	6.75	148.31	101.96		$-3.32 \pm^{0.36}_{0.29}$	$0.79 \pm^{0.15}_{0.19}$	0.02
				King model					
All	$6.18 \pm^{0.07}_{0.07}$	$9.50 \pm^{0.11}_{0.11}$	6.53	67.51	46.42	1			
bMS	$6.81 \pm^{0.04}_{0.05}$	$9.76 \pm^{0.10}_{0.10}$	6.71	80.65	55.45	1			
rMS	$6.53 \pm^{0.07}_{0.07}$	$10.11 \pm^{0.12}_{0.12}$	6.95	78.39	53.90	1			
				Wilson model					
All	$5.35 \pm^{0.07}_{0.08}$	$9.31 \pm^{0.11}_{0.11}$	6.40	145.58	100.08	2			
bMS	$6.07 \pm^{0.04}_{0.05}$	$9.36 \pm^{0.11}_{0.09}$	6.44	224.43	154.26	2			
rMS	$5.60 \pm^{0.06}_{0.06}$	$9.76 \pm^{0.11}_{0.11}$	6.71	174.27	119.80	2			

REFERENCES

Alfaro-Cuello, M., Kacharov, N., Neumayer, N., et al. 2019, ApJ, 886, 57

Amaro-Seoane, P., Konstantinidis, S., Brem, P., & Catelan, M. 2013, MNRAS, 435, 809

Anderson, J. 2002, in Astronomical Society of the Pacific Conference Series, Vol. 265, Omega Centauri, A Unique Window into Astrophysics, ed. F. van Leeuwen, J. D. Hughes, & G. Piotto, 87

Balbinot, E. & Gieles, M. 2018, MNRAS, 474, 2479

Bedin, L. R., Piotto, G., Anderson, J., et al. 2004, ApJL, 605, L125

Bekki, K. & Freeman, K. C. 2003, MNRAS, 346, L11

Bekki, K. & Norris, J. E. 2006, ApJL, 637, L109

Bekki, K. & Tsujimoto, T. 2016, ApJ, 831, 70

Bellini, A., Anderson, J., Bedin, L. R., et al. 2017a, ApJ, 842, 6

Bellini, A., Anderson, J., van der Marel, R. P., et al. 2017b, ApJ, 842, 7

Bellini, A., Milone, A. P., Anderson, J., et al. 2017c, ApJ, 844, 164

Bellini, A., Piotto, G., Bedin, L. R., et al. 2009, A&A, 507, 1393

Bianchini, P. 2019, arXiv e-prints, arXiv:1909.07275

Braga, V. F., Stetson, P. B., Bono, G., et al. 2016, AJ, 152, 170

Calamida, A., Bono, G., Stetson, P. B., et al. 2007, ApJ, 670, 400

Calamida, A., Bono, G., Stetson, P. B., et al. 2009, ApJ, 706, 1277

Calamida, A., Stetson, P. B., Bono, G., et al. 2005, ApJL, 634, L69

Calamida, A., Strampelli, G., Rest, A., et al. 2017, AJ, 153, 175

Cannon, R. D. & Stobie, R. S. 1973, MNRAS, 162, 207

Carballo-Bello, J. A., Corral-Santana, J. M., Martínez-Delgado, D., et al. 2017, MNRAS, 467, L91

Cardelli, J. A., Clayton, G. C., & Mathis, J. S. 1989, ApJ, 345, 245

Carretta, E., Gratton, R. G., Lucatello, S., et al. 2010, ApJL, 722, L1

Carretta, E., Lucatello, S., Gratton, R. G., Bragaglia, A., & D'Orazi, V. 2011, A&A, 533, A69

Castellani, V., Calamida, A., Bono, G., et al. 2007, ApJ, 663, 1021

Claydon, I., Gieles, M., Varri, A. L., Heggie, D. C., & Zocchi, A. 2019, MNRAS, 487, 147

Claydon, I., Gieles, M., & Zocchi, A. 2017, MNRAS, 466, 3937

Da Costa, G. S. & Coleman, M. G. 2008, AJ, 136, 506

Dalessandro, E., Cadelano, M., Vesperini, E., et al. 2018, ApJ, 859, 15

de Boer, T. J. L., Gieles, M., Balbinot, E., et al. 2019, MNRAS, 485, 4906

del Pino, A., Hidalgo, S. L., Aparicio, A., et al. 2013, MNRAS, 433, 1505

Fabrizio, M., Nonino, M., Bono, G., et al. 2015, A&A, 580, A18

Ferraro, F. R., Bellazzini, M., & Pancino, E. 2002, ApJL, 573, L95

Ferraro, F. R., Massari, D., Dalessandro, E., et al. 2016, ApJ, 828, 75

Ferraro, F. R., Sollima, A., Pancino, E., et al. 2004, ApJL, 603, L81

Gaia Collaboration, Helmi, A., van Leeuwen, F., et al. 2018, A&A, 616, A12

Gavagnin, E., Mapelli, M., & Lake, G. 2016, MNRAS, 461, 1276

Geyer, E. H., Hopp, U., & Nelles, B. 1983, A&A, 125, 359

Gieles, M. & Zocchi, A. 2015, MNRAS, 454, 576

Harris, W. E. 1996, AJ, 112, 1487

Hilker, M. & Richtler, T. 2000, A&A, 362, 895

Ho, N., Geha, M., Tollerud, E. J., et al. 2015, ApJ, 798, 77

Ibata, R., Bellazzini, M., Malhan, K., Martin, N., & Bianchini, P. 2019, arXiv e-prints

Ibata, R. A., Wyse, R. F. G., Gilmore, G., Irwin, M. J., & Suntzeff, N. B. 1997, AJ, 113, 634

Johnson, C. I. & Pilachowski, C. A. 2010, ApJ, 722, 1373

Jurcsik, J. 1998, ApJL, 506, L113

Kayser, A., Hilker, M., Richtler, T., & Willemsen, P. G. 2006, A&A, 458, 777

King, I. R. 1966, AJ, 71, 64

Kuzma, P. B., Da Costa, G. S., & Mackey, A. D. 2018, MNRAS, 473, 2881

Law, D. R., Majewski, S. R., Skrutskie, M. F., Carpenter, J. M., & Ayub, H. F. 2003, AJ, 126, 1871

Lee, J.-W. 2015, ApJS, 219, 7

Leon, S., Meylan, G., & Combes, F. 2000, A&A, 359, 907

Makino, J., Akiyama, K., & Sugimoto, D. 1991, Ap&SS, 185, 63

Marconi, M., Musella, I., Di Criscienzo, M., et al. 2014, MNRAS, 444, 3809

Marino, A. F., Milone, A. P., Piotto, G., et al. 2009, A&A, 505, 1099

Marino, A. F., Milone, A. P., Piotto, G., et al. 2011, ApJ, 731, 64

Martínez-Vázquez, C. E., Monelli, M., Gallart, C., et al. 2016, MNRAS, 461, L41

Mastrobuono-Battisti, A., Khoperskov, S., Di Matteo, P., & Haywood, M. 2019, A&A, 622, A86

Mayor, M., Duquennoy, A., Udry, S., Andersen, J., & Nordstrom, B. 1996, in Astronomical Society of the Pacific Conference Series, Vol. 90, The Origins, Evolution, and Destinies of Binary Stars in Clusters, ed. E. F. Milone & J.-C. Mermilliod, 190

Milone, A. P., Marino, A. F., Bedin, L. R., et al. 2017, MNRAS, 469, 800

Monelli, M., Pulone, L., Corsi, C. E., et al. 2003, AJ, 126, 218

Norris, J. E. & Da Costa, G. S. 1995, ApJ, 447, 680

Norris, J. E., Freeman, K. C., Mayor, M., & Seitzer, P. 1997, ApJL, 487, L187

Norris, J. E., Freeman, K. C., & Mighell, K. J. 1996, ApJ, 462, 241

Olszewski, E. W., Saha, A., Knezek, P., et al. 2009, AJ, 138, 1570

Pancino, E., Ferraro, F. R., Bellazzini, M., Piotto, G., & Zoccali, M. 2000, ApJL, 534, L83

Pancino, E., Galfo, A., Ferraro, F. R., & Bellazzini, M. 2007, ApJL, 661, L155

Pancino, E., Seleznev, A., Ferraro, F. R., Bellazzini, M., & Piotto, G. 2003, MNRAS, 345, 683

Pasquato, M. & Chung, C. 2016, A&A, 589, A95

Piotto, G., Villanova, S., Bedin, L. R., et al. 2005, ApJ, 621, 777

Platais, I., Wyse, R. F. G., Hebb, L., Lee, Y.-W., & Rey, S.-C. 2003, ApJL, 591, L127

Saha, A., Olszewski, E. W., Brondel, B., et al. 2010, AJ, 140, 1719

Schechter, P. L., Mateo, M., & Saha, A. 1993, PASP, 105, 1342

Schlafly, E. F. & Finkbeiner, D. P. 2011, ApJ, 737, 103

Searle, L. & Zinn, R. 1978, ApJ, 225, 357

Smith, V. V., Suntzeff, N. B., Cunha, K., et al. 2000, AJ, 119, 1239

Sollima, A., Bellazzini, M., Smart, R. L., et al. 2009, MNRAS, 396, 2183

Sollima, A., Ferraro, F. R., & Bellazzini, M. 2007a, MNRAS, 381, 1575

Sollima, A., Ferraro, F. R., Bellazzini, M., et al. 2007b, ApJ, 654, 915

Sollima, A., Ferraro, F. R., Pancino, E., & Bellazzini, M. 2005a, MNRAS, 357, 265

Sollima, A., Pancino, E., Ferraro, F. R., et al. 2005b, ApJ, 634, 332

Suntzeff, N. B. & Kraft, R. P. 1996, AJ, 111, 1913

Thurl, C. & Johnston, K. V. 2002, in Astronomical Society of the Pacific Conference Series, Vol. 265, Omega Centauri, A Unique Window into Astrophysics, ed. F. van Leeuwen, J. D. Hughes, & G. Piotto, 337

Trager, S. C., King, I. R., & Djorgovski, S. 1995, AJ, 109, 218

van de Ven, G., van den Bosch, R. C. E., Verolme, E. K., & de Zeeuw, P. T. 2006, A&A, 445, 513

Wilson, C. P. 1975, AJ, 80, 175

Yong, D. & Grundahl, F. 2008, ApJL, 672, L29